JM PAPERS

The modulation of coherent structures by the near-wall motions of particles

Yuen Feng[1], Hongyou Liu[1,†] and Xiaojing Zheng[2]

[1]Center for Particle-Laden Turbulence, Lanzhou University, Lanzhou 730000, PR China
[2]Research Center for Applied Mechanics, Xidian University, Xi'an 710071, PR China

Particle–wall interaction generates strong particle near-wall motion, including collision bounce and impact splashing. To distinguish the effect of particles and particle near-wall motions on the turbulent coherent structure, this study carried out three different cases of sand-laden two-phase flow measurements: a uniform sand release at the top, local-laying sand bed and global-laying sand bed (Liu *et al.*, *J. Fluid Mech.*, vol. 943, 2022, A8). Based on large field of view particle image velocimetry/particle tracking velocimetry measurements, we obtained the velocity field of a two-dimensional gas–solid two-phase dilute faction flow ($\Phi_v \sim O(10^{-4})$)) with a friction Reynolds number Re_τ of 3950. Results indicate that particles weaken the high- and low-velocity iso-momentum zones and hairpin vortices, resulting in the increased length scale of the coherent structure. However, the collision bounce and impact splashing break up the inner iso-momentum zone and hairpin vortices while enhancing them in the outer region, thus reducing the structure scale. In addition, the upward-moving particles increase the large-scale structure inclination angle, while the downward-moving particles decrease it. The linear coherence spectrum analysis suggests that the particles themselves do not change the structural self-similarity, but their saltation motions disrupt the similarity of the near-wall structure, making the inclination angle decrease with the scale, and the generated ascending particles reduce the aspect ratio of the streamwise to wall-normal direction in the outer region.

Key words: particle/fluid flow, turbulent boundary layers

1. Introduction

Coherent structures represent a series of organised motions in random and complex turbulent signals (Dennis 2015), which generally include near-wall streaks, hairpin/quasistreamwise vortices, large-scale motions (LSMs) and very-large-scale

† Email address for correspondence: liuhongyou@lzu.edu.cn

motions (VLSMs) (Marusic *et al.* 2010). According to Smith (1984), the low-speed streaks and hairpin vortices are interlinked. The unstable shear layer at the top of the low-speed streaks oscillates to roll up the vortex, and the vortex moves outward and downstream (due to the velocity gradient) to form the hairpin vortices. The low-speed streaks themselves are generated and maintained by the remnants of hairpin legs, which remain close to the wall and are stretched into counter-rotating quasistreamwise vortices. The presence of approximately regular low-speed streaks in wall turbulence was confirmed by Kline *et al.* (1967) via hydrogen bubble tracing with a length of $1000\nu/u_\tau$ and a spacing of $100\nu/u_\tau$ (where ν is the air kinematic viscosity and u_τ is the friction velocity). The basic idea of the hairpin vortex packet model suggests that hairpin vortices are aligned consistently along the flow direction, forming hairpin vortex packets called LSMs, which are typically δ (where δ is thickness of turbulent boundary layer) in length (Kim & Adrian 1999; Adrian, Christensen & Liu 2000; Motoori & Goto 2019, 2021). Their heads are inclined to the wall along an angle θ, which is usually considered to be a large-scale structure inclination angle, where $12° < \theta < 20°$. Multiple large-scale structures constitute the VLSMs through a concatenation mechanism (Kim & Adrian 1999; Adrian *et al.* 2000; Dennis & Nickels 2011*a*; Lee & Sung 2011; Wu, Baltzer & Adrian 2012; Deshpande, de Silva & Marusic 2022), typically with a length more than 3δ; i.e. multiple large-scale heads and tails aligning in the streamwise direction, meandering in the spanwise (Hutchins & Marusic 2007; Deshpande, Monty & Marusic 2019).

Following the discovery of coherent structures, various models have been developed to understand the statistical behaviour of coherent motions in turbulent flows. A phenomenological model that has been extensively studied is Townsend's attached eddy hypothesis (AEH). The AEH suggests that the energetic eddies in the logarithmic region are self-similar, attach to the wall and are stochastically distributed in a hierarchical form (Perry & Chong 1982). The similarity of wall-attached coherent structures has been shown to exist in wall turbulence through the methods of spectrum-based scale decomposition and clustering algorithm (Del Álamo *et al.* 2006; Lozano-Durán, Flores & Jiménez 2012; Baars, Hutchins & Marusic 2017*b*; Hwang & Sung 2018; Marusic & Monty 2019; Hu, Yang & Zheng 2020; Deshpande *et al.* 2021). The aspect ratios of streamwise/wall-normal and spanwise/wall-normal are found to be 14 : 1 and 1 : 1, respectively (Baars *et al.* 2017*b*; Baidya *et al.* 2019). Meanwhile, the self-similar structures are all scaled to less than 10δ (Baars *et al.* 2017*b*), and the thermal stability reduces the aspect ratio of streamwise/wall-normal (Krug *et al.* 2019; Li *et al.* 2022). In addition, similarities also exist in the inclination angle of structures at different scales (Baars, Hutchins & Marusic 2017*a*; Li *et al.* 2022), i.e. the inclination angle is the same among different scales. However, in two-phase flow, particle effects on the aspect ratio of coherent structures have yet to be studied.

Two-phase flows are prevalent in nature, and the study of the interaction between particles and coherent structures facilitates a more insightful understanding of gas–solid two-phase flows. The effect of particles on the modulation of the turbulent coherent structure depends on many factors, such as particle size, particle Stokes number St^+ ($St^+ = \tau_p/\tau_f$, where $\tau_p = \rho_p d_p^2/(18\rho_f\nu)$ refers to the relaxation time of the particles, and $\tau_f = \nu/u_\tau^2$ is the turbulent viscous time scale, ρ_p and ρ_f are the density of particles and fluid, respectively), particle volume fraction (Φ_v)/mass fraction (Φ_m), roughness, sedimentation, and particle–wall collisions, etc. For small particles (with size d_p smaller than the Kolmogorov scale η), numerous numerical studies have been devoted to particle modulation of coherent structures by point-particle large eddy simulation and direct numerical simulation (PP-DNS) (Portela & Oliemans 2003; Dritselis & Vlachos 2008;

Zhao, Andersson & Gillissen 2010; Dritselis & Vlachos 2011; Lee & Lee 2015). Existing studies show that the particle St^+ is critical for the modulation of the coherent structure (Dritselis & Vlachos 2011). When $St^+ < 1$, the particles become energy sources, inhibiting the stability of the streaks and resulting in more quasistreamwise vortices with enhanced intensity (Lee & Lee 2015). Conversely, when $St^+ > 1$, the particles become energy sinks, strengthening the stability of the streaks and thus reducing the generation of streamwise vortices (Dritselis & Vlachos 2008, 2011; Zhao *et al.* 2010; Li *et al.* 2012) with weakened intensity (Portela & Oliemans 2003; Dritselis & Vlachos 2008) but unchanged inclination angle (Dritselis & Vlachos 2008; Li *et al.* 2012; Liu, Luo & Fan 2016). In addition, both small and large St^+ particles enhance the VLSMs, but follow different mechanisms: the small St^+ particles indirectly enhance the VLSMs by enhancing the self-sustaining mechanism of LSMs near the wall, while the large St^+ particles increase the contribution of the Reynolds shear stress in the outer region, directly promoting the VLSMs (Wang & Richter 2019). However, for large particles ($d_p > \eta$), due to the limitation of PP-DNS, a method of particle-resolved DNS was applied (Kidanemariam *et al.* 2013; Picano, Breugem & Brandt 2015). Large particles generate wake eddies in the flow field and consequently increase the mean diameter and spacing of the quasistreamwise vortices (Kidanemariam *et al.* 2013; Picano *et al.* 2015) but reduce the spanwise distance of the streaks (Luo *et al.* 2017), which is different from that of small particles.

As for particles with different $\Phi_m \setminus \Phi_v$, Picano *et al.* (2015) employed four-way coupled fully resolved DNS in a Reynolds number $Re_\tau = u_\tau \delta / \nu = 180$ horizontal channel with $\Phi_v = 0.05$, 0.1 and 0.2, and suggested that particles increased the mean diameter and spacing of the quasistreamwise vortices, and the effect was enhanced by increasing Φ_v. Tay, Kuhn & Tachie (2015) applied fluorescence particle image velocimetry (PIV) to a two-phase channel flow with $\Phi_v = (2\text{–}8) \times 10^{-4}$ and a $Re_\tau = 444.5$. The result demonstrated that particles increase the length scale and inclination of LSMs, and the enhancement is more pronounced with higher Φ_v. However, the interface-resolved DNS of Costa, Brandt & Picano (2021) at $Re_\tau = 180$ indicated that the particles do not affect the coherent structure at low particle volume fraction ($\Phi_v = 3 \times 10^{-5}$), while destroying them significantly at high volume fraction ($\Phi_v = 3 \times 10^{-3}$). With the consideration of gravity in relatively high $\Phi_m \setminus \Phi_v$ and low-velocity two-phase flow, the strong particle settling effect forms a settlement layer on the wall surface (Shao, Wu & Yu 2012; Ji *et al.* 2014), which serves as a roughness wall with vortex shedding on the surface (Yang, Chung & Nepf 2016; Kidanemariam & Uhlmann 2017; Scherer *et al.* 2022), leading to enhanced strength and widened spacing of the near-wall streaks (Jie *et al.* 2022; Rohilla, Arya & Goswami 2023).

In addition to the particle dimensionless parameters, the particle–wall collision significantly affects the modulation of coherent structures. For example, the PIV experiment in a horizontal channel by Li *et al.* (2012) found that the particle trajectory cross-over effect (Righetti & Romano 2004) generated by frequent particle–wall collisions promotes the breaking of the near-wall streaks and quasistreamwise vortex. Subsequently, Lee & Lee (2019) investigated two-phase flow in a horizontal channel with $Re_\tau = 180$ through PP-DNS and found that the low-speed streaks and quasistreamwise vortex were attenuated as the particles collided with the wall. Since VLSMs play a dominant role in the outer region of wall turbulence, Zheng, Wang & Zhu (2021) explored the effects of top-released and local-laying particles on the VLSMs, and results indicated that the collision bounce of particles damaged the near-wall VLSMs. Recently, Gao, Samtaney & Richter (2023) revealed that the particle settling leads to a collision with the wall, reducing the length and inclination angle of LSMs/VLSMs while widening the spanwise width via PP-DNS in a gas–solid two-phase flow with $Re_\tau \approx 5200$.

In nature, there are usually erodible beds in both wind-blown sand flows and sandstorms. The settling particles impact the erodible surface, not only rebounding but also splashing the surrounding stationary particles, while only collision bounces occur when particles interact with solid walls. Here, the collision bounce and impact splashing are collectively referred to as particle near-wall motions. The existing studies indicate that both the two-phase flows with and without particle near-wall motions have effects on coherent structures. However, previous studies seldom distinguished the effects of different degrees of particle near-wall motions. Moreover, the impacts of collision bounce and impact splashing on coherent structures are not refined. Therefore, this study aims to address this aspect by designing four comparative cases of large field-of-view (FOV) PIV/particle tracking velocimetry (PTV) wind tunnel experiments with the same incoming velocity, including particle-free and particle-laden flows with three different modes of sand release (top-release particles, local-laying sand bed and global-laying sand bed). These three cases of particle-laden flows have similar particle volume fractions but different degrees of particle near-wall motions.

This paper is organised as follows. Section 2 describes the experimental set-up and data processing. The particles and particle near-wall motion effects on the characteristics of coherent structures are provided in §§ 3, 4 and 5, where § 3 presents the instantaneous velocity clouds, two-point correlation contour maps and instantaneous hairpin vortices and the joint probability density functions (j.p.d.f.s) of the particle and gas phase velocities. Section 4 discusses the change in the scale and inclination angle. Section 5 describes the self-similarity inferred from the linear coherence spectra (LCSs). Finally, the conclusions are summarised in § 6.

2. Experimental settings and treatment

The experiments were carried out in the multifunctional environmental wind tunnel laboratory at Lanzhou University, and the experimental set-up was described in detail by Liu, Feng & Zheng (2022). Therefore, only a brief description is provided in this section. The wind tunnel working section has a cross-section of 1.3 m × 1.4 m with a length of 20 m. The measurement location for this experiment was at 7.5–9 m downstream of the beginning of the working section (as presented in figure 1), where the incoming velocity was fixed at $U_\infty = 9.0$ m s^{-1}, and the corresponding incoming turbulence intensity was approximately 1 %. The origin of the PIV/PTV measurement was placed on the floor; x, y, and z denote the streamwise, wall-normal and spanwise directions, respectively. The corresponding three components of velocity are noted as U, V, W, where u, v, w are the fluctuating velocities, respectively. The friction velocity u_τ expresses the inner-scale unit, the viscous scale ν/u_τ is denoted as $(.)^+$ and the outer-scale unit is the boundary layer thickness δ.

For consistency and simplicity of reading, the particle-free condition is denoted as case 1. A schematic diagram of the experimental set-up for three different cases of particle-laden flows is shown in figure 1. For case 2 in figure 1(*a*), the particles were uniformly dropped from the top of the wind tunnel entrance through the feed system at a distance of 8 m from the shooting region. The particles were accelerated by the free stream while settling to enter the boundary layer and collide with the wall. The estimated impact point based on particle size and settling velocity ranged from 3.4 to 14.3 m, as shown in the light pink region in figure 1(*a*); that is, the large particles reach the wall at approximately 3.4 m downstream of the entrance while it is at 14.3 m downstream for small particles. Thus, small particles might fly out of the shooting region, and only large particles collided
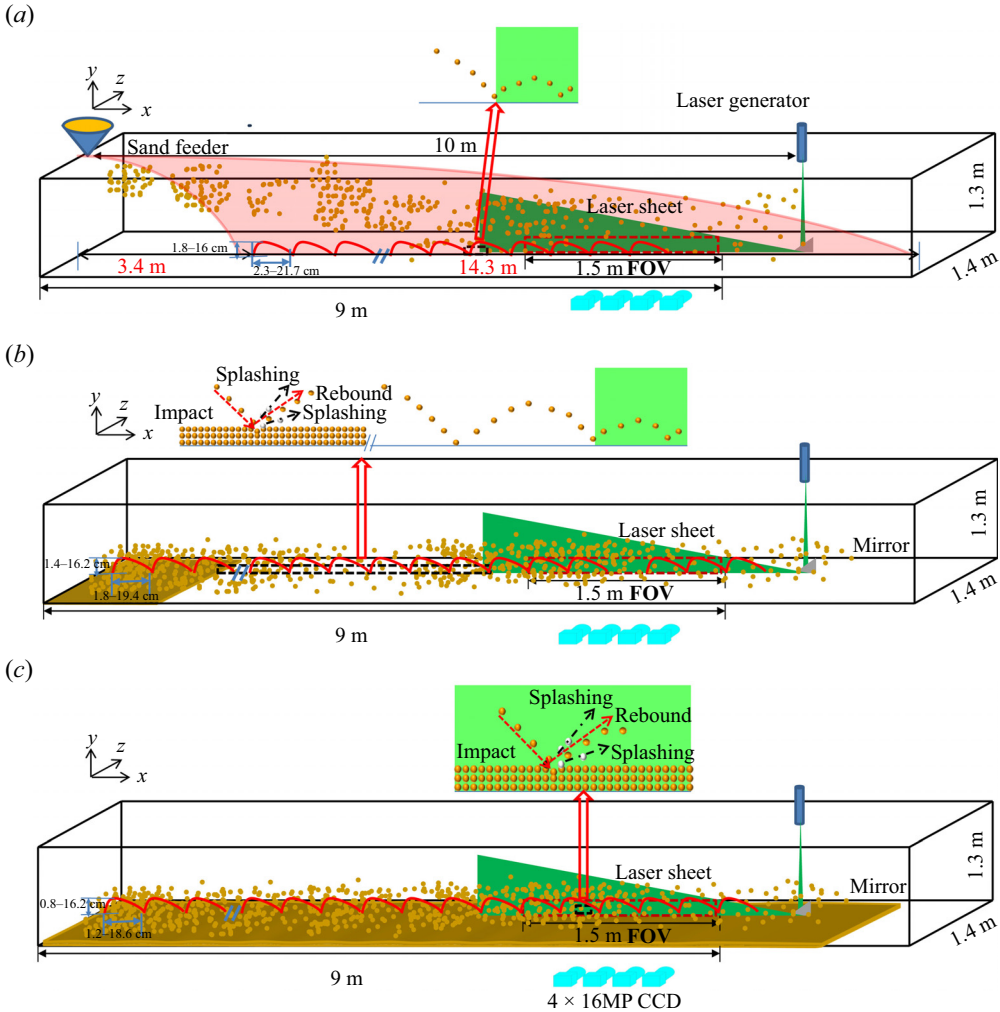
Figure 1. Experimental set-up: schematic diagram of experimental settings for (*a*) uniform top-release sand from the ceiling of the tunnel, (*b*) local-laying sand bed and (*c*) global-laying sand bed.

and rebounded with the wall in the measurement area, forming saltation movement. Based on the empirical formula provided by Pähtz & Tholen (2021), the saltation heights and lengths of particles with different sizes were approximately 1.8–16 cm and 2.3–21.7 cm, respectively (shown by the red solid line in figure 1*a*). In case 3 (figure 1*b*), a sand bed of 1.3 m × 1 m × 0.02 m was placed at the beginning of the wind tunnel working section. All the different-sized particles were entrained by the flow field from the local-laying sand bed, colliding with and rebounding from the solid wall frequently before entering the field of view. The estimated saltation heights and lengths were 1.4–16.2 cm and 1.8–19.4 cm, respectively. The frequency and intensity of the collision bounce were significantly greater than that of the top-release particle in case 2. In case 4 (figure 1*c*), the global-laying sand bed was spread uniformly in the working section of the wind tunnel with a size of 10 m × 1 m × 0.05 m. The sand particles were bottom released, similar to case 3, with saltation heights and lengths of 0.8–16.2 cm and 1.2–18.6 cm, respectively. However, different from case 3, the collision of particles against the erodible surface not only had

its own rebound but also splashed other surrounding stationary particles, which made the frequency of particle–wall collisions higher and the saltation trajectory more complex (see supplementary movie at https://doi.org/10.1017/jfm.2024.65).

In case 1 and case 2, PIV sampling was conducted continuously with no breaks. For case 3 and case 4, since the sand layer was carried away by the incoming flow, the whole sampling process was divided into 16 runs of 200 image pairs. Within each run (duration of 50 s), the sand surface was lowered by 0.002 m. Before each run, the lost sand particles on the bed are re-supplied and smoothed to maintain the consistency of the sand bed in each run without modifying the inlet conditions. The equivalent sand-grain roughness height $k_s^+ \approx 40$ was estimated in case 4 following Ligrani & Moffat (1986), which suggests that the bed surface could be in the transitionally rough regime ($2.25 \leqslant k_s^+ \leqslant 90$). The roughness in a transitionally rough regime does not affect the two-point correlation, similarity, etc. (Volino, Schultz & Flack 2007; Wu & Christensen 2010). Moreover, according to Kadivar, Tormey & McGranaghan (2021), the roughness sublayer of case 4 is approximately (2–3) $k_s^+ \approx 80$–120, which is lower than the height we are concerned with in the present work, and thus does not affect the results either. In the two-phase flows, size-selected sand particles from the Tengger Desert, with a density $\rho_p = 2600$ kg m^{-3} and diameter $d_p = 203 \pm 95$ µm (mean $\pm$ standard deviation) are used in this study. The particle diameter ranges from 30 to 480 µm and the particle size distribution can be found in Liu *et al.* (2022). Here, we calculate the particle parameters using the average size of the particles (Zheng *et al.* 2021; Zhu *et al.* 2021; Liu *et al.* 2022). The bulk volume fractions of particles in case 2–case 4 that are obtained by the ratio of the particle volume to the total field of view are 1.1×10^{-4}, 1.4×10^{-4} and 1.5×10^{-4}, respectively. These volume fractions lie within the two-way coupling range ($10^{-6} < \Phi_v < 10^{-3}$), indicating that particles have significant feedback on turbulent motion and interparticle collisions are negligible (Elghobashi 1994).

The velocity fields of the particle-laden flows were obtained by simultaneous PIV/PTV measurements. A laser with an energy output of 500 mJ per pulse of 532 nm green light formed a shaping sheet of light to illuminate the streamwise/wall-normal plane, and then diethylhexyl sebacate oil droplets of 0.3–3 µm particle size were uniformly released into the wind tunnel to track the gas phase velocity. Four charge-coupled devices (CCDs) were placed side by side to acquire the two-dimensional flow field along the flow direction at 4 Hz, each with a resolution of 4920×3280 pixels. With a 50 mm Nikon lens mounted in front of each CCD and a focal length set to f#4, this multicamera set-up provided a larger field of view, $\Delta X \times \Delta Y = 1.50$ m $\times$ 0.25 m or $8\delta \times 1.4\delta$, for simultaneous resolution of small structures, LSMs and VLSMs, enabling the simultaneous study of different structure scales.

In this study, there was a significant difference in the size of the tracer particles and sand particles, and the images were processed by median filtering according to the phase separation method (Kiger & Pan 2000). The tracer particles are obtained through a high-pass filter (2×2 pixels), while sand particles are acquired by a low-pass filter kernel (5×5 pixels). Due to the strong reflection of the sand particles, particles out of the plane may also be illuminated. By counting the brightness of the particles in the field of view, the majority of the particles had a brightness value higher than 400. Therefore, we identified particles with a grey value higher than 400 as in-plane particles. For the gas phase pictures, an adaptive PIV algorithm of Dantec software was employed to calculate the velocity. An interrogation window of 32×32 pixels and 75 % overlap area was applied, yielding 64 viscous units per vector and each vector had a spacing of 16 viscous units. The final statistics of the 3200 pairs of pictures yielded convergence of the mean velocity with a

relative error less than 1 %. The overall mean uncertainty of the deviations in velocity calculated with 95 % confidence intervals was less than 2 %. However, the errors in the near-wall region are significantly larger than those in the outer region. The uncertainties are approximately less than ± 2.0 % in case 2, ± 3.2 % in case 3 and ± 7.3 % in case 4 close to the wall ($y^+ > 50$), while the errors decrease to 0.84 %, 0.73 % and 0.68 % for case 2–case 4 away from the wall, respectively. These errors are consistent with the particle-laden turbulent boundary layer (TBL) result in Zhu *et al.* (2019) (1 %) and channel flow in Tay *et al.* (2015) (3 %), suggesting the reliability of the present experimental data. For the particle phase, a high-accuracy hybrid PTV–PIV algorithm was employed to calculate the position and velocity of the particles (detailed in Liu *et al.* 2022). The uncertainties of particle mean velocities in all particle-laden flows are less than 1 % when the image numbers reach the order of 10^5.

The velocity profiles obtained for case 1 were fitted to obtain the corresponding flow field friction Reynolds number. Here, the boundary layer thickness and friction velocity were obtained by the chart method of Clauser (1956) with log-law constants of $\kappa = 0.41$ and $B = 5.0$. Here, u_τ is 0.355 m s^{-1} and δ is 0.187 m. The obtained mean velocity profiles and streamwise turbulent fluctuation intensity were consistent with existing theoretical results (Liu *et al.* 2022). As for the particle-laden flow, the particle affects both the friction velocity and the von Kármán constant (Li & McKenna Neuman 2012; Revil-Baudard *et al.* 2016), there is a large uncertainty in the estimation of friction velocity. To ensure comparability, the incoming velocity was set to a constant value, i.e. $U_\infty = 9.0$ m s^{-1}; thus, the background flow field was consistent for the four cases. Following previous experimental studies on turbulence modification in gas–particle flows, such as Zhang, Wang & Lee (2008), Li *et al.* (2012) and Zheng *et al.* (2021), we apply the friction velocity in case 1 to the particle-laden cases for the inner scale dimensionless. Additionally, the thickness of the boundary layer may change with the change in roughness (Volino *et al.* 2007; Wu & Christensen 2010). Here, we used δ_{99} (the height where the boundary layer velocity reaches 99 % of the free-stream value) as the boundary layer thickness, which were approximately 0.187 m, 0.185 m, 0.192 m and 0.202 m. The outer scaling was normalised by the boundary layer thickness of each case. The key boundary layer parameters of the sand-free and sand-laden flows are shown in table 1. The particle Reynolds number obtained by the slip velocity was $Re_p = d_p|u_f - u_p|/\nu \sim O(10^0 - 10^1)$ for three cases of particle-laden flows. The particle Stokes number $St^+ = \tau_p/\tau_f \sim O(10^2 - 10^3)$, was estimated from the modified particle relaxation time $\tau_p = \rho_p d_p^2/(18\nu\rho_f(1 + 0.15Re_p^{0.687}))$ and the turbulent viscous time scale $\tau_f = \nu/u_\tau^2$. The values of St corresponding to the Kolmogorov time scale $\tau_l = (\nu/\varepsilon)^{1/2}$ (ε is the turbulence dissipation ratio which was calculated according to the large eddy PIV method proposed by Sheng, Meng & Fox 2000) and the time scale of the energetic turbulent eddy $\tau_L \approx \delta/(0.1U_\infty)$ are denoted as St_l and St_L, respectively. Here, St_l and $St_L \sim O(10^0 - 10^1)$ meant that the inertia and gravity of the particles could not be neglected.

The local particle volume fraction was performed with a traditional boxing counting method. The total measurement region was divided into many small regions with a size of $\Delta x \times \Delta y = 12$ mm $\times$ 1 mm ($\Delta x^+ \times \Delta y^+ = 252 \times 21$). The local mean particle volume fraction was $\Phi_{local}(x, y) = V_p N(\Delta x, \Delta y, t)/(\Delta x \Delta y \Delta z)$. Each subinterval has a 50 % overlap area in the streamwise direction. Here, V_p is the particle volume, and $N(x, y)$ is the number of particles in the sub-region; Δz is the thickness of the laser sheet (approach to 1 mm) and t is the time of the particle's snapshot. The local volume fractions of sand grains at different wall-normal distances are normalised via the integrated concentration

	u_τ (m s^{-1})	y_0 (mm)	δ_{99} (m)
Case 1	0.355	—	0.187
Case 2	0.422	0.78	0.185
Case 3	0.562	0.83	0.192
Case 4	0.632	1.33	0.202

Table 1. Key boundary layer parameters of the sand-free and sand-laden flows. The friction velocity and the aerodynamic roughness lengths were obtained by the Clauser method.
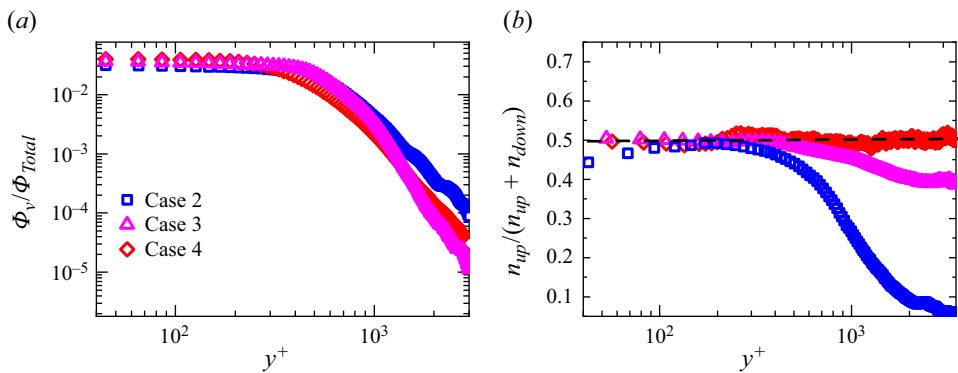

Figure 2. Particle distributions at different inner-scaled wall-normal distances: (*a*) particle volume fraction Φ_v normalised with the integrated concentration over y^+ (denoted as Φ_{total}); (*b*) the ratio $n_{up}/(n_{up} + n_{down})$, where n_{up} and n_{down} are the numbers of ascending and descending particles, respectively.

over y^+ (denoted as Φ_{total}), as shown in figure 2(*a*). Figure 2(*a*) shows that the variations of $\Phi_{local}/\Phi_{total}$ with y^+ collapse reasonably well with each other in the near-wall region and log region for particle-laden flows. This offers a convincing premise for the comparison analyses undertaken subsequently. The local volume fraction in the tunnel ranges from 10^{-3} to 10^{-6}, which corresponds to a two-way coupling (Elghobashi 1994).

The near-wall motions are mainly reflected in the generation of the ascending particles. Therefore, the ratio of the ascending particle number (n_{up}) to the total particle number ($n_{up} + n_{down}$) can be employed to quantify the degree of particle near-wall motions in different cases of sand-laden flows, as shown in figure 2(*b*). As expected, there is a remarkable difference in the ratio of $n_{up}/(n_{up} + n_{down})$ in the outer region (approximately $y^+ > 300$) for three cases of sand-laden flows. In case 2–case 4, the proportion of ascending particles in the outer region increased successively, suggesting a continuously increasing degree of particle near-wall motions. In case 2, small particles did not collide with the wall within the field of view, only large particles did (as described in figure 1*a*). This results in a smaller ratio of upwards-moving particles in the outer region; that is, the particle near-wall motions were weak in this case. However, in case 3, as displayed in figure 1(*b*), the particles were entrained by the flow to a high position, and then underwent a collision bounce with the wall under gravity, after several times of collision bounces, reaching the shooting field of view. Hence, the collision bounce was enhanced in case 3 when compared with that in case 2. In case 4, the particle near-wall motions are the most violent because the addition of impact splashing produced more ascending particles compared with case 2 and case 3. Therefore, the influence of particles on the coherent

981 A26-8

structure can be illustrated by comparing the results of case 1 and case 2, a comparison of case 2 and case 3 can be used to clarify the collision bounce effects and the results in case 3 are compared with those in case 4 to explore the effects of impact splashing. Although there are significant differences in the degree of particle near-wall motions in case 2–case 4, the proportions of ascending particles are generally consistent near the wall ($y^+ < 300$).

3. Two-dimensional profile morphology of large-scale structures

The instantaneous velocity maps of the u-component for the four cases are shown in figure 3. As depicted in figure 3, in case 1, the flow field has a wall-attached organisation with periodic alternating positive and negative fluctuations along the flow direction, which is consistent with the results of numerical simulations (Dennis & Nickels 2011*a*,*b*) and experimental observations (de Silva *et al.* 2020; Deshpande *et al.* 2022). Established results demonstrate that alternating periodic coherent structures can decompose attached coherent structures, detached turbulent vortex structures and other structures (Baars & Marusic 2020*a*,*b*; Wang *et al.* 2022). In case 2, while the high- and low-velocity zones remain, the intensity of the iso-momentum zone is significantly lower throughout the boundary layer compared with that of case 1, indicating that the turbulent fluctuation intensity is reduced in the top-release particle two-phase flow, which is consistent with the decreased turbulent intensity provided in Liu *et al.* (2022). In the outer region, the particle near-wall motions are relatively weak. The organisation of this positive and negative alternating periodic wall-attached iso-momentum zone remains, but becomes less pronounced, suggesting that the particles do not significantly alter the distribution patterns of high- and low-velocity iso-momentum zones but reduce their intensities. In case 3 and case 4, the alternating positive and negative high- and low-velocity zone structures are observable in the outer region and are significantly stronger, especially in case 4, than those in case 2. However, the high- and low-velocity zones are almost non-existent near the wall, indicating that the wall-attached self-similar coherent structure is significantly damaged. In the inner region, the particle volume fractions and the ratio of the ascending particle number in case 2–case 4 are similar (as shown in figure 2), but the saltation trajectories exhibit significant differences (as depicted in figure 1). Hence, we can speculate that the complex saltation trajectory leads to this difference; that is, the disruption of structures near the wall can potentially result from frequent particle–wall collisions, which inhibit the burst process in the near-wall region. In the outer region, the ratios of upward-moving particles in case 2–case 4 are increased successively, promoting the upward transport of the near-wall turbulent kinetic energy, which is responsible for the significantly stronger iso-momentum zone in case 3 and case 4. This is consistent with the pre-multiplied spectrum result in Liu *et al.* (2022), that the ascending particles produced by particle near-wall motions promote upward transport, lifting the VLSMs further from the wall and making them more energetic. To summarise, particles weaken the intensity of the high- and low-velocity iso-momentum zones, while the collision bounce and the impact splashing enhance and lift them. Nevertheless, frequent particle–wall collisions and complex saltation motions disrupt the wall-attached structure in the inner region.

To further illustrate the modulation of particles and particle near-wall motion on the coherent structure, the two-point cross-correlation graphs at two different reference heights (near-wall region $y/\delta < 0.1$ and wake region $y/\delta > 0.3$) are calculated, and the results are displayed in figures 4 and 5. The cross-correlation $R_{u_1u_2}$ between any two velocity
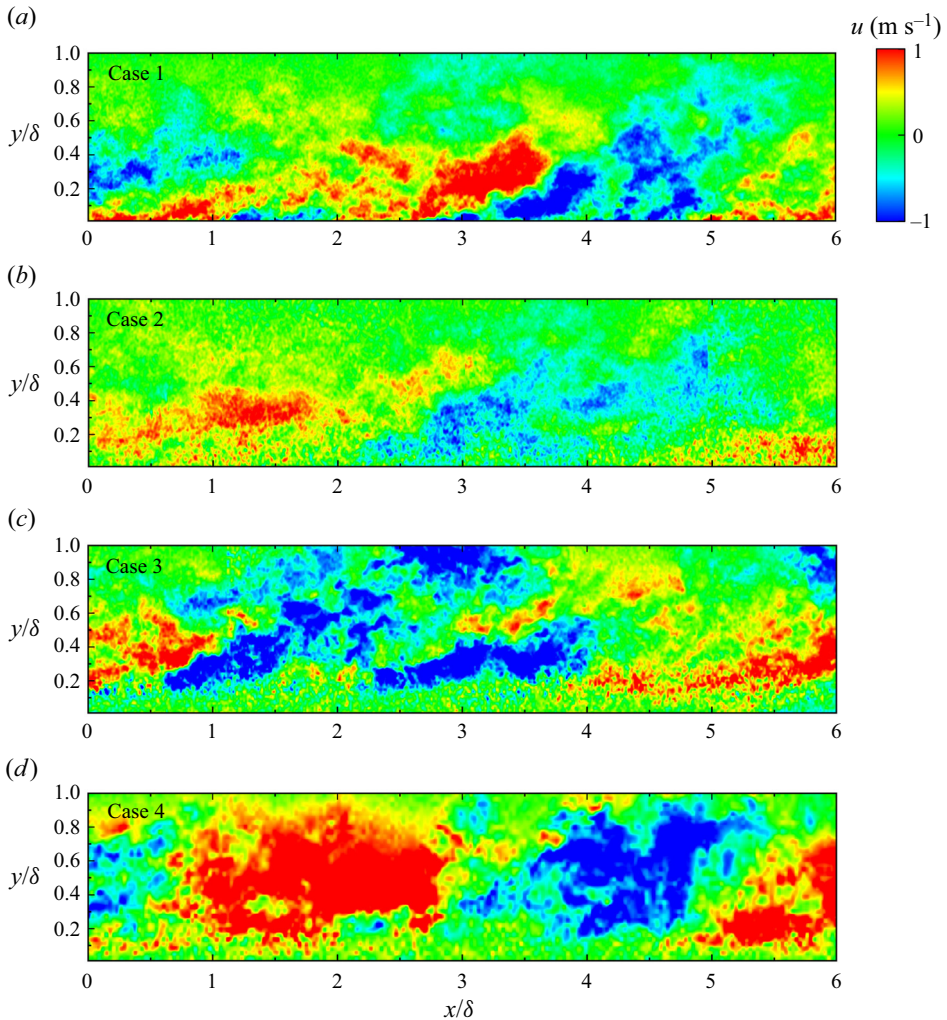
Figure 3. The streamwise instantaneous velocity clouds for cases 1–4; these are displayed in (*a–d*), respectively.

fluctuations $u_1(x, y)$ and $u_2(x, y)$ is calculated as follows:

$$R_{u_1 u_2} \left(x_{ref} + \Delta x, y_{ref} + \Delta y \right) = \frac{\left\langle u_1 \left(x_{ref}, y_{ref} \right) u_2 \left(x_{ref} + \Delta x, y_{ref} + \Delta y \right) \right\rangle}{\left\langle \sigma_{u_1} \left(x_{ref}, y_{ref} \right) \sigma_{u_2} \left(x_{ref} + \Delta x, y_{ref} + \Delta y \right) \right\rangle}, \quad (3.1)$$

where (x_{ref}, y_{ref}) shows the selected reference position point, Δx and Δy mean the streamwise and wall-normal distances from the reference point and σ_{u_1} and σ_{u_2} represent the mean root square of the velocity fluctuations u_1 and u_2, respectively.

Figure 4 plots the two-point cross-correlations of streamwise velocity fluctuations in four cases of experiments in the near-wall region (at reference height $y_{ref} \approx 0.03\delta$ and $y_{ref}^+ = 120$); the two-point correlation threshold is $R_{uu} > 0.15$ and the contour levels are from 0.15 to 0.95 in increments of 0.2. The two-point correlation map displays the size of the coherent structure (Moin & Kim 1985; Bhaganagar, Kim & Coleman 2004). Therefore, the change in cloud size can reflect the modulation degree of the structure by the particles.
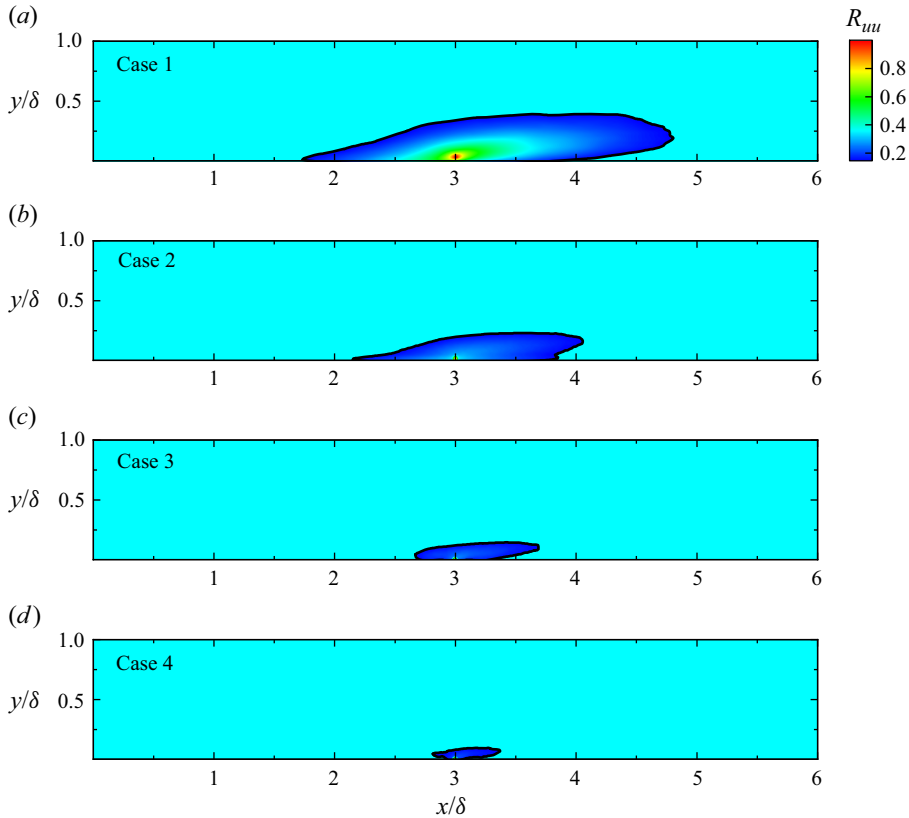
Figure 4. Two-point cross-correlation of streamwise velocity fluctuations at a reference height $y_{ref} \approx 0.03\delta$ ($y_{ref}^+ = 120$) for case 1–case 4 illustrated in (*a*–*d*), respectively. Contour levels are from $R_{uu} = 0.15$ to 0.95 in increments of 0.2.

In case 1, there is a coherent structure in the TBL flow that is inclined in line with the flow direction. The correlation region in the streamwise direction exceeds 3δ, indicating that inclined very-large-scale coherent structures are the dominant structure feature in the single-phase flow. This agrees well with the existing results in the particle-free TBL (Adrian *et al.* 2000; Hutchins & Marusic 2007; Tay *et al.* 2015; Zheng *et al.* 2021). In case 2, the length scale of the coherent structure is reduced when compared with that in case 1. Although the particle near-wall motion is relatively weak in case 2, numerous upward-moving particles are inevitably retained near the wall. Therefore, it is difficult to distinguish whether the particle or particle near-wall motions reduce the structural scale. However, the result in case 2 is different from the increased structural scale by the suspended particle which exhibits negligible interaction with the wall (Tay *et al.* 2015), but consistent with that of Zheng *et al.* (2021) in the flow with particle near-wall motions. Hence, we can infer that the particle collision bounce causes the length scale of the coherent structure to decrease. In the near-wall region, the ratio of ascending particles is the same for both case 3 and case 2, but the length scale of the structure in case 3 is further decreased. This may be because the particle–wall collisions are more frequent in case 3. Therefore, the frequent particle–wall collisions also enhance the reduction of the length scale of the structure. Compared with case 3, case 4 has an erodible surface, which contains the collision bounce and the additional impact splashing. The splashing particle
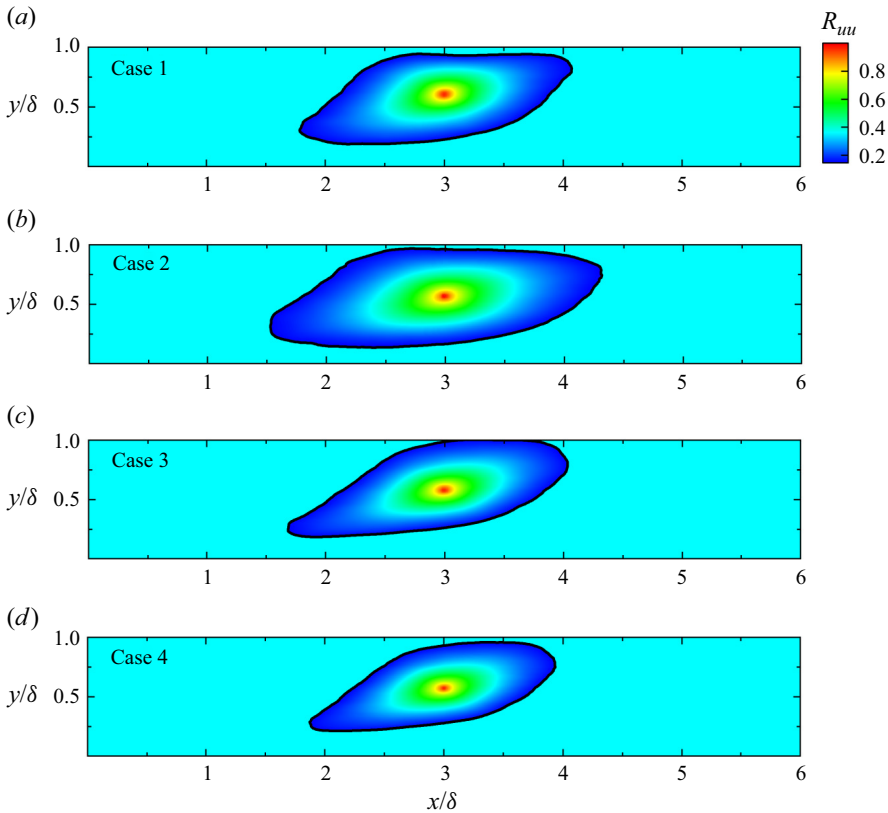
981 A26-11

Figure 5. Two-point cross-correlation of streamwise velocity fluctuations at a reference height $y_{ref} = 0.55$–0.6δ. Cases 1–4 are illustrated in (*a–d*), respectively. The contour levels are from $R_{uu} = 0.15$ to 0.95 in increments of 0.2.

makes particle–wall collisions more frequent and saltation trajectories more complicated. As a result, the decreased length scale of the coherent structure is more pronounced.

Figure 5 plots the two-point correlation maps of particle-laden and unladen flows in the wake region (at reference height $y_{ref} = 0.55$–0.6δ, $y^+ = 2370$), with colour map levels ranging from 0.15 to 0.95 in an increment of 0.2. In case 1, the coherent structure in the wake region is slightly reduced compared with those in the logarithmic layer, which is in qualitative agreement with the existing results in particle-free flows (Tomkins & Adrian 2003; Tay *et al.* 2015; Zheng *et al.* 2021); the coherent structures that exist in the logarithmic region do not retain their coherence in the wake region (Marusic 2001) and thus reduce the streamwise length scale. In case 2, however, the length scale increased compared with case 1, which is contrary to the reduced structure of the near-wall region (e.g. figure 5*a*). This is because in the top-release particle case, the proportion of ascending particles decreases dramatically in the outer region, and the descending particles dominate. The descending particles accelerate the flow while the ascending particles with lower velocities decelerate it close to the wall (Liu *et al.* 2022). This implies that the velocity gradient is increased, and the mean shear is enhanced. Following the theory of hairpin vortex packets (Adrian *et al.* 2000), LSMs are composed of multiple hairpin vortices. The enhanced velocity gradient leads to an increase in the spacing of hairpin vortices at different flow layers (the older hairpins move downstream faster than the younger hairpins

981 A26-12

in the same packet). In other words, the enhanced mean shear more significantly stretches the vortex packet. Therefore, the length scale of VLSMs/LSMs is increased. This means that, in top-release particle two-phase flows, the descending particles increase the length scale of the coherent structure, agreeing with the results of Tay *et al.* (2015). Both case 3 and case 4 have higher ratios of ascending particle than case 2, and the degree of particle near-wall motions is gradually enhanced, resulting in a decrease in the length scale of structure in both case 3 and case 4.

Combining the results in figures 4 and 5 indicates that, in the weaker particle near-wall motion cases, the large number of descending particles makes the turbulence velocity gradient increase, which enhances the vortex packet stretching, thereby making for an increase in the length scale of the structure. The ascending particles generated by the particle near-wall motions disrupt the coherence of the fluid, causing a decreased structural scale. Additionally, the more frequent the collisions of particles with the wall, the more complex the trajectories of the saltation particles, and the more significant the damage to the structure.

Previous studies have shown that the hairpin vortices are regularly arranged on large packets, and their generation, growth and dissipation play an essential role in energy transfer and matter transport (Adrian *et al.* 2000). Furthermore, the arrangement of the hairpin vortices also reflects the distribution of the LSMs in the TBL. There are several methods for identifying hairpin vortices: the Q criterion (Hunt, Wray & Moin 1988), the λ_2 criterion (Jeong & Hussain 1995) and the swirling strength λ_{ci} criterion (Zhou *et al.* 1999). In this study, we utilise the swirling strength λ_{ci} criterion of the spanwise vortices to identify the vortex core; specifically, the magnitude of the imaginary part of the complex eigenvalue of the local velocity gradient tensor is considered to be the swirling strength of the vortex (Zhou *et al.* 1999; Hutchins, Hambleton & Marusic 2005; Wu & Christensen 2006).

Since the swirling strengths are all positive and do not identify the direction of swirl, Wu & Christensen (2006) proposed to replace the swirling strengths with the following equation:

$$\Lambda_{ci,z} = \lambda_{ci,z}\left(\omega_z/|\omega_z|\right), \tag{3.2}$$

where ω_z is the fluctuating vorticity in the plane, $\Lambda_{ci} < 0$ indicates a prograde spanwise vortex and $\Lambda_{ci} > 0$ indicates a retrograde spanwise vortex. The identification of individual vortex boundaries using λ_{ci} requires a suitable threshold. Here, we choose a threshold that is identical to Wu & Christensen (2006), minimising the effect of the experimental noise associated with the velocity gradient.

Figure 6 displays the instantaneous vortices swirling strength clouds in particle-free and particle-laden flows, with case 1–case 4 shown by figures 6(*a*)–6(*d*), respectively. A uniform convection velocity ($U_c = 0.8U_\infty$ in four cases, where U_∞ is the free-stream velocity) is removed from each field to reveal those vortices whose cores are advecting at this velocity. The blue zone in the graphs represents the prograde spanwise vortex swirling intensity, and the red zone stands for the retrograde spanwise vortex swirling intensity. In figure 6(*a*), the field contains many prograde spanwise vortex cores, which are associated with the heads of hairpin vortices advecting in the streamwise direction (Adrian *et al.* 2000). The low-velocity fluid under and upstream of the prograde spanwise vortex is lifted away from the wall (often referred as a Q_2 event), coinciding with hairpin vortex characteristics observed by Adrian *et al.* (2000) and Wu & Christensen (2006). Several streamwise vortices are arranged along the dashed red line superimposed on the streamwise velocity field, forming a hairpin vortex packet. The inclination angle of this
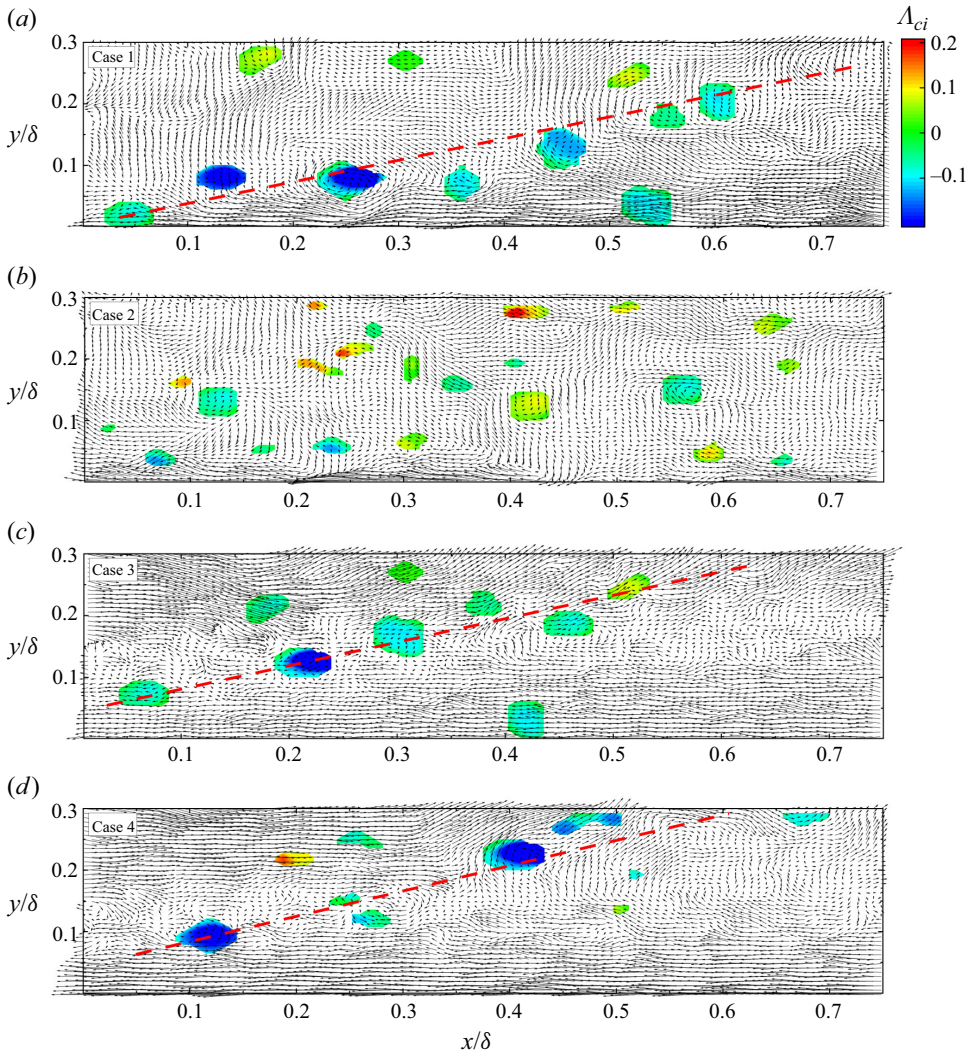
Figure 6. The Galilean decomposition of this instantaneous field is based on a convection velocity of $0.8U_\infty$. Instantaneous hairpin vortex maps for four cases; cases 1–4 are displayed in (*a–d*), respectively.

vortex packet to the wall is approximately $12°$, which is consistent with the vortex packet angle of the particle-free flow in Christensen & Adrian (2001).

A comparison of figures 6(*a*) and 6(*b*) indicates that the instantaneous hairpin vortex structures were significantly changed in case 2. Although the number of vortices is increased, their strength is generally weakened compared with those in case 1. In the case of the top-release particle, the ratio of ascending particles decreases sharply with the wall-normal distance. This suggests that the descending particles weaken the strength of the vortices, which can also be supported by the observation in Liu *et al.* (2022) that the descending particles suppress the Q_2 and Q_4 events. In case 3, the number of the vortices decreases considerably near the wall while their intensity is significantly enhanced in the outer region in figure 6(*c*) compared with that in case 2. In the inner region, as described in figure 6(*b*), the ratio of the upward-moving particle is the same in both cases of sand-laden
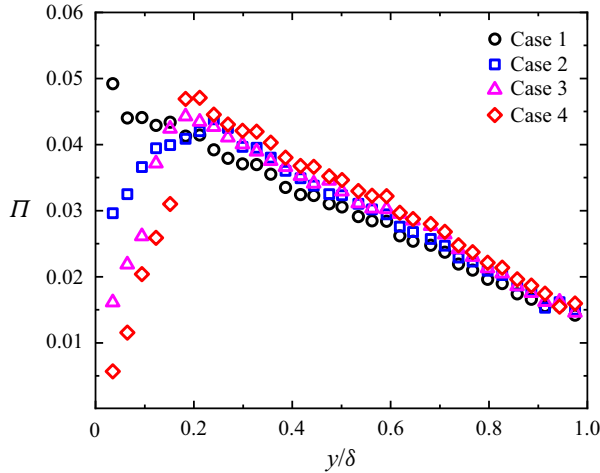
981 A26-14

Figure 7. Prograde and retrograde vortex population densities in the outer scaling for cases 1–4.

flows, but the particle–wall collisions are more frequent in case 3 when compared with these in case 2. Therefore, the frequent particle–wall collisions contribute to the decreased number of hairpin vortex structures. In the outer region, the ratio of ascending particles is larger in case 3 than in case 2. The ascending particles promote the upward transport of energy, which enhances the strength of vortices. This process is consistent with the enhanced outer spectral peak observed in Liu *et al.* (2022). The vortex packet remaining in case 3 is inclined at approximately 15° to the wall (as the red dashed lines in figure 6*c*). In case 4, compared with case 3, the additional impact splashing makes the particle–wall collisions more frequent, the saltation trajectory more complex and the ratio of upward particles more significant. These result in the less near-wall vortices and more remarkable enhanced strength of vortices, as shown in figure 6(*d*).

To provide more statistical analysis to back up the results in figure 7, the population density distributions of the hairpin vortices with the wall-normal distance are investigated in all of the four cases of the experiments. Due to the discrete nature of the spatial distribution of hairpin vortex structures, this study adopts a method similar to Wu & Christensen (2006) to calculate the distribution of the vortex population density (Π) with height. The specific formula is given as

$$\Pi = \frac{N(y/\delta)}{\dfrac{\Delta y}{\delta} \dfrac{L_x}{\delta}}. \tag{3.3}$$

Here, N is the number of the vortices, $\Delta y/\delta$ is the height of the box and L_x/δ is the length of the box, L_x is the streamwise field of view in this study and Δy is the height difference between the neighbouring boxes. The streamwise length is much larger than its vertical height and generally comparable to the boundary layer thickness.

The resulting population density distributions of the hairpin vortices for the four cases are shown in figure 7. As expected, the results of the particle-free flow shown by the black symbols (case 1) decrease significantly with height. This is consistent with the attached vortex theory as well as the results given by Wu & Christensen (2006) in the particle-free flow. However, the overall trend of all of the three cases of particle-laden flows is quite different from the tendency of monotonically decreasing in the particle-free

flow. The population densities in case 2–case 4 follow the trend of first increasing and then decreasing with the wall-normal distance. The population densities of near-wall vortices in the sand-laden flow are considerably lower than that in the sand-free case. This is because the ratio of ascending particles near the wall is large in all three cases of sand-laden flows (as shown in figure 2*b*). Specifically, the near-wall vortex population density decreases sequentially in case 2, case 3 and case 4. This is because the frequency of particle–wall collisions increases sequentially in case 2–case 4 close to the wall, and the saltation trajectories become more and more complex. This provides statistical evidence supporting the results in figure 6. In addition, the slightly decreased population density in the particle-free flow compared with that in particle-laden flows may be because particles induce movement of surrounding fluids.

The vortex generated by shear (hairpin vortex or quasistreamwise vortex in Townsend 1976) causes the lower-velocity fluids to throw up and the higher velocity fluids to sweep down ('ejection' and 'sweep' events in Jeong *et al.* 1997), causing the streamwise and vertical fluctuating velocities to generally distribute over the Q_2 and Q_4 quadrants. Therefore, the quadrant analysis can be used as a representation of the vortex generated by shear. Figures 8(*a*)–8(*c*) represent the j.p.d.f.s of particle and gas phase velocities in case 2–case 4 in the inner ($y/\delta = 0.045$–0.05, $y^+ = 197.5$) and outer ($y/\delta = 0.16$–0.20, $y^+ = 790$) regions, respectively. In case 2, the j.p.d.f.s of the gas phase resemble an ellipse in both the near-wall and outer regions, and thus 'ejection' and 'sweep' events dominate these regions. This result is in accordance with available particle-laden flow results with negligible near-wall motions (Kiger & Pan 2002; Marchioli & Soldati 2002; Li *et al.* 2012; Zhu *et al.* 2019; Berk & Coletti 2020; Baker & Coletti 2021). The general morphologies of the j.p.d.f.s of the particle phase in the inner and outer regions both tilt towards the Q_2 and Q_4 quadrants as with that of the gas phase. The top-released particles are accelerated by the fluid, entering the boundary layer and forming the particle cluster structure due to the influence of the turbulent coherent structure (Zhu *et al.* 2021; Cui, Ruhman & Jacobi 2022). Although the particles finally collide with the wall, they still maintain the structural characteristics of the flow field; hence showing the phenomenon of tilting towards Q_2 and Q_4 quadrants. It is noted that the enhancing trend of the Q_4 event is caused by the occurrence probability of the downward-moving particle becoming dominant.

In case 3 and case 4, the j.p.d.f.s of the gas and particle phase velocities exhibit a relatively uniform quadrant distribution in the inner region, while showing a preferential distribution towards Q_2 and Q_4 quadrants in the outer region. Near the wall, the bottom-released particles initially collide with the wall frequently at the entrance of the working section of the wind tunnel, destroying the generation of vortices and reducing 'ejection' and 'sweep' events. In the outer region, the particles carried by the gas phase show a fluid-like particle cluster structure under the influence of the flow field, resulting in the significant 'ejection' and 'sweep' events. Moreover, the ascending particles generated by the collision bounce, especially the impact splashing, enhance the upward transport of the energy, making the fluctuation intensity of the gas phase be augmented successively in case 2–case 4. The statistics in figure 8 provided further evidence supporting the qualitative result in figures 3–6.

The above results further indicate that the particles weaken the hairpin vortices. Nevertheless, the collision bounces and splashing action against the wall break down the hairpin vortex structures attached to the wall while strengthening the turbulent vortex structures away from the wall.
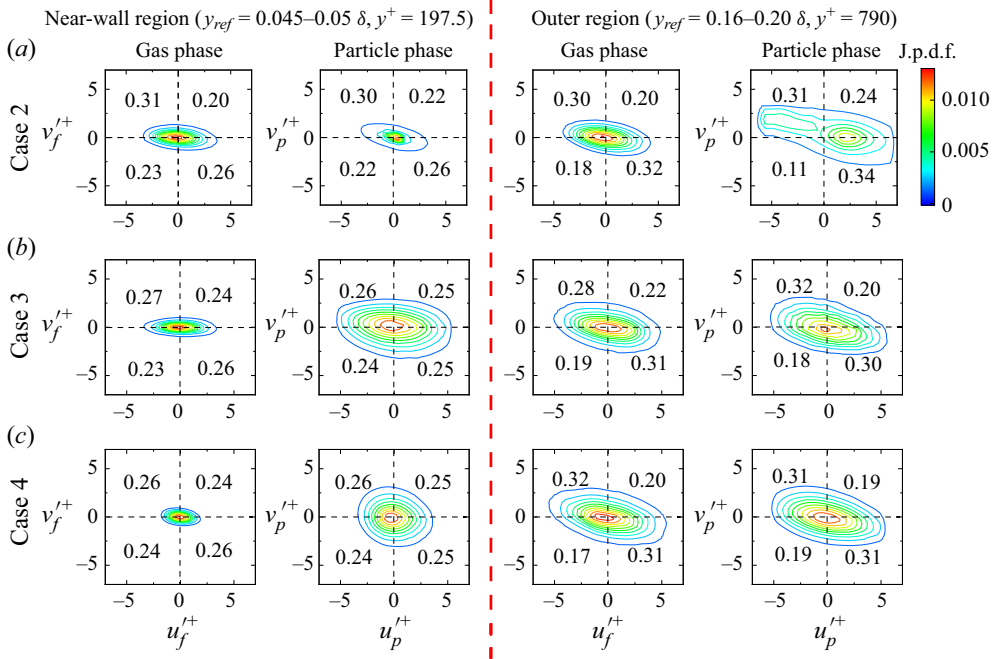
Figure 8. The j.p.d.f.s at $y/\delta = 0.045$–0.05 ($y^+ = 197.5$) and $y/\delta = 0.16$–0.20 ($y^+ = 790$) for the two-dimensional velocities in the particle-laden flows. Panels (*a*–*c*) represent the results of cases 2–4, respectively. The corresponding probability in each quadrant is shown to reflect the joint contribution of the entire quadrant.

4. Scale and inclination of large-scale structures

Figure 9(*a*) plots the autocorrelation diagram in the particle-free case at a reference position close to the wall ($y_{ref} = 0.05\delta$). It is seen in figure 9(*a*) that the present experimental results (shown by the red line) are in good agreement with the previously documented data (shown by the symbols) at $Re_\tau = 7610$, $14\,380$ and $19\,960$ (Hutchins & Marusic 2007). This verifies the reliability of the calculation methods and the results in this study.

To extract the length scale of the large-scale coherent structure, the two-point correlation threshold coefficient was set to $R_{uu} = 0.15$ (shown by the grey line in figure 9*a*). The resulting structural scales at different reference heights (y_{ref}) in case 1–case 4 are shown in figure 9(*b*). The scale of the coherent structure in the particle-free flow of case 1 gradually increases with the wall-normal distance and approaches a peak at approximately the top of the logarithmic layer, while it decreases as y_{ref} continues to increase in the wake region. This trend is generally consistent with the available laboratory TBL results in single-phase flows (Hutchins & Marusic 2007; Tutkun *et al.* 2009), as shown by the grey symbols. The overall tendency in case 2–case 4 is in agreement with that of the sand-free flow, but there is a significant quantitative difference. Near the wall, the length scale of coherent structure in case 2–case 4 is reduced in sequence. As mentioned in § 3, although the ratios of ascending particles in sand-laden cases are close to each other, their saltation motions exhibit a significant difference, and thus show different degrees of reduction of the length scale of the coherent structure. Away from the wall, the ratio of ascending particles in case 2 is decreased and then the motion of descending particles dominates the
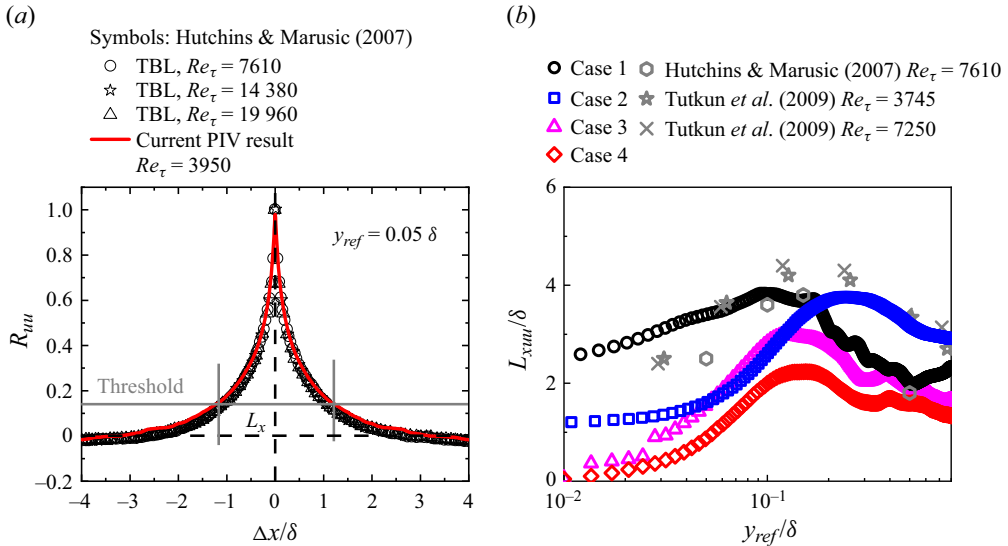
Figure 9. (*a*) Autocorrelation of the particle-free velocity fluctuations at the reference height ($y_{ref} = 0.05\delta$). The circles, stars and triangles are the results of the Hutchins & Marusic (2007) at friction Reynolds numbers of 7610, 14 380 and 19 960, respectively. (*b*) Variation in the structure length scale with height in four cases. The results of case 1–case 4 are represented by the black circle, blue square, pink triangle and red diamond in the diagram, respectively. The grey hexagons indicate the results of Hutchins & Marusic (2007) at $Re_\tau = 7610$, while grey pentagrams and crosses indicate the result of Tutkun *et al.* (2009) at $Re_\tau = 3745$ and 7250.

flow, resulting in an increase in the structural scale. Furthermore, the peak in case 2 is located further away the wall ($y_{peak} \approx 0.3\delta$), which is consistent with the results of Tay *et al.* (2015) in particle-laden flows with negligible particle–wall interaction (approximate $y_{peak} \approx 0.3\delta$). As for case 3 and case 4, the significant particle near-wall motions (still large ratio of upward-moving particles in the outer region) make the length scale shorter than the particle-free results.

Figure 10(*a*) displays the two-point correlations of the streamwise velocity fluctuations at the reference height ($y_{ref} = 0.05\delta$) with that at the rest of the wall-normal locations. It is evident that the correlation peak decreases with increasing height and there is a displacement offset in the peak location away from $\Delta x = 0$ (shown by black dots in figure 10*a*), which is denoted as Δx^*. Then, the peak offsets at different heights are fitted using the least squares method (Volino, Schultz & Flack 2009; Wu & Christensen 2010) to obtain the structure inclination angle, i.e. $\theta = \arctan(\Delta y / \Delta x^*)$.

By applying the calculating procedure of θ to all of the four cases of particle-laden and unladen flows, the mean inclination angles of the coherent structures at different heights were statistically obtained, and the results are represented in figure 10(*b*). In case 1 (black circles), the structure inclination angles in the particle-free case increase with the height, and θ is approximately $15°$ in the near-wall region. This is consistent with the trend in the particle-free flow (Marusic 2001; Wu & Christensen 2010; Liu, Bo & Liang 2017).

In all of the three particle-laden cases, the overall trend of θ changing vs y^+ is generally consistent with that in case 1, but there is a remarkable difference in the magnitude of the angle. Specifically, the structure inclination angle in case 2 is the smallest among all of the four cases. In case 2, the sand particles were released uniformly from the ceiling of the wind tunnel. Therefore, the number of descending particles is much larger than the ascending particles. The descending particles exert a downward force on the coherent
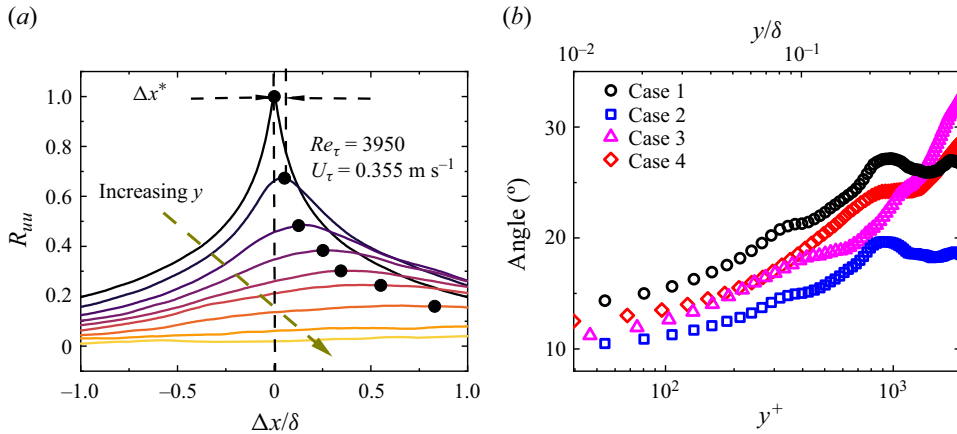
981 A26-18

Figure 10. (*a*) Correlation between the velocity fluctuations at different heights and velocity fluctuations at reference points ($y_{ref} = 0.05\delta$). (*b*) Variation in the structure inclination with height at different reference points. The results of case 1–case 4 are represented by the black circle, blue square, pink triangle and red diamond in the diagram, respectively.

structure and cause a 'pushing' effect, changing the orientation of the large-scale structure and leading to a decrease in the inclination angle. In another aspect, as mentioned in the description of figure 5, the descending particles enhance the mean shear of the flow. The enhanced shear more significantly stretches the hairpin vortex packet, and thus the large-scale structure is more elongated with a smaller tilt. This result can also be verified according to the parameterised equation for the inclination angle vs the friction velocity proposed in Liu *et al.* (2017).

In case 3, as shown by the pink upper triangles in figure 10, the inclination angle in the whole boundary layer is larger than that in case 2. Given the more frequent particle–wall collision and larger proportion of ascending particles in case 3 than in case 2, it may be suitable to suggest that the ascending particle causes a 'lifting' effect and thus increases the structure inclination angle. This may be further supported by the slightly increased angles in case 4 (red diamonds), because the addition of the impact splashing effect further increases the upward motion of the particles. Therefore, the inclination angle is modulated by the dynamic process of both upward-moving and downward-moving particles. The upward-moving particles increase the inclination angle of the LSM, while the downward-moving particles decrease it.

In addition, as described in §2, the roughness of the erodible bed surface in case 4 lies in the transitional roughness regime. The existing results show that the effect of the rough wall on the inclination angle is not significant, even with a fully rough surface (Wu & Christensen 2010). Therefore, in this study, the effect of roughness can be neglected, and the main factor leading to the change of the inclination angle is the motions of the particles.

5. Self-similarity of coherent structures

Section 4 quantifies the mean scale and inclination angle of the coherent structure. In wall turbulence, however, the coherent structures exhibit multiscale characteristics. Some geometric and physical commonalities inhabit the multiscale structures, such as the
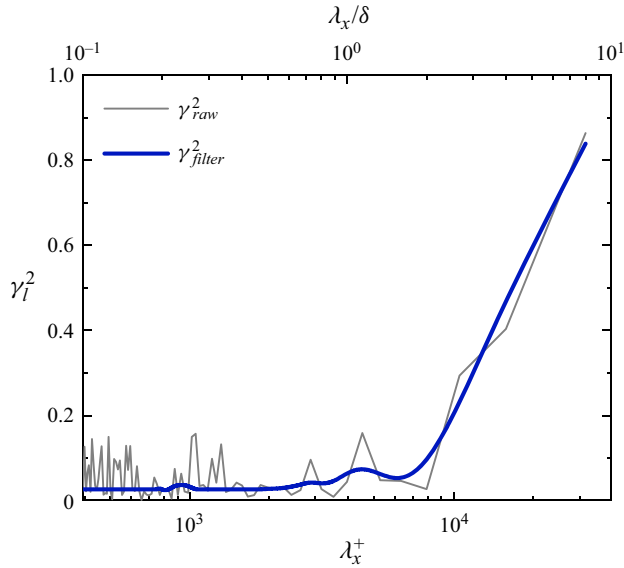
Figure 11. The LCS of the velocity fluctuation in case 1 at $y/\delta == 0.05\delta$, with the filtered LCS ($\gamma^2_{l\ filter}$, solid blue line) constructed from the original LCS ($\gamma^2_{l\ raw}$, solid grey line) using a 30 % BMF.

self-similarity. Therefore, it is necessary to further study the effects of different degrees of particle near-wall motions on the self-similarity of multiscale turbulent structures.

To examine the structural self-similarity, the LCS is a commonly used method, which is calculated as (Baars, Hutchins & Marusic 2016; Baars *et al.* 2017*a*,*b*; Baidya *et al.* 2019; Baars & Marusic 2020*a*; Li *et al.* 2022),

$$\gamma^2_l \left(y, y_{ref}; \lambda_x\right) \equiv \frac{\left|\left\langle \hat{U}\left(y; \lambda_x\right) \hat{U}'\left(y_{ref}; \lambda_x\right)\right\rangle\right|^2}{\left\langle \left|\hat{U}\left(y; \lambda_x\right)\right|^2\right\rangle \left\langle \left|\hat{U}'\left(y_{ref}; \lambda_x\right)\right|^2\right\rangle}, \tag{5.1}$$

where $\hat{U}(y, \lambda_x) = F[u(x)]$ is the Fourier transform of $u(x)$, $\langle.\rangle$ denotes the ensemble average, the superscript '$'$' is the complex conjugate, $|.|$ denotes the modal length and $\lambda_x = L_x/n$ (L_x is the length of the field of view, n the number of equal spacings) is the wavelength. Here, LCS is the square of the magnitude of the cross-spectrum. This study used an overlap of 50 % with $N = 2^8$ sample times, each subset of approximately 4 data points, to ensure the convergence of the spectral statistics at the maximum wavelength. Figure 11 plots a raw coherence spectrum $\gamma^2_{l\ raw}$ and a filtered map $\gamma^2_{l\ filter}$. For the latter, a similar treatment to that in Baars *et al.* (2016) was used, with a 30% bandwidth moving filter (BMF), implying that the $\gamma^2_{l\ filter}$ is equal to the mean of the unfiltered spectra in the range, $\lambda_x \pm 30\%$.

According to the results of Baars *et al.* (2017*b*), LCSs collapse well in the logarithmic region of $3Re_\tau^{1/2} < y^+ < 0.15Re_\tau$ at different Reynolds numbers in boundary layer flows. The γ^2_l value in the large-scale range of $\delta < \lambda_x < 10\delta$ exhibits a log–linear relationship with λ_x/y. Subsequently, Baars & Marusic (2020*a*) found that the overlap of the LCSs was unrelated to the reference height but was associated with the distance between two correlated heights ($\Delta y = y - y_{ref}$). The magnitude of the LCS in the log region follows

981 A26-20

the logarithmic scaling law

$$\gamma_l^2 = C_1 \ln\left(\frac{\lambda_x}{\Delta y}\right) + C_2, \tag{5.2}$$

where C_1 and C_2 denote the fitted parameters. The least squares fit of the experimental results was performed, and C_1 and C_2 were determined to be 0.302 and -0.795, respectively, which is in good agreement with the coefficients ($C_1 = 0.302$ and $C_2 = -0.798$) in Baars & Marusic (2020*a*).

Therefore, we obtain a streamwise and wall-normal aspect ratio (AR) as follows:

$$AR = \left.\frac{\lambda_x}{\Delta y}\right|_{\gamma_l^2=0} = \exp\left(\frac{-C_2}{C_1}\right). \tag{5.3}$$

Figure 12 represents the LCSs for case 1 to case 4 with different reference heights ($y_{ref} = 0.03\delta, 0.10\delta, 0.15\delta$ and 0.20δ). In figure 12(*a*), the LCSs collapse well in the large-scale range and satisfy the logarithmic scaling at all of the different reference heights. The resulting streamwise/wall-normal ARs are approximately 14 and do not vary with the reference height. This value is consistent with the results in the existing single-phase flow experiments (Baars *et al.* 2017*a*; Baars & Marusic 2020*a*), further illustrating the reliability of the present experimental results.

In case 2, the LCSs at different heights exhibit a widening dispersion when the reference heights lower than 0.15δ. The corresponding ARs of the VLSMs/LSMs are no longer consistent at different wall-normal distances (as illustrated in the first two diagrams of figure 12*b*), i.e. the self-similarity of the multiscale structure is not satisfied. As described in figures 4 and 7, the near-wall collision bounce in case 2 suppresses the generation of hairpin vortices; thus, the wall-attached structures are destroyed, reducing the length scale and making the ARs no longer the same at different heights. In the outer region (as shown by the last two subgraphs in figure 12*b*), the LCSs that are above the reference height overlapped again, satisfying the scaling law $\gamma_l^2 = 0.302 \ln(\lambda_x/\Delta y) - 0.795$ (as dashed lines shown in figure 12*b*). Then, we obtained the streamwise/wall-normal ARs of approximately 14. This indicates that the self-similar coherent structure remained in the outer region of $y/\delta \geqslant 0.15\delta$. Combining with the results in § 3, it is suggested that the descending particles weaken the strength of the positive and negative alternating periodic iso-momentum zone and hairpin vortices but do not change the self-similarity.

Figures 12(*c*) and 12(*d*) display the LCSs at different reference heights in case 3 and case 4, respectively. The widening dispersion of LCSs at different heights is lifted to the reference height of 0.15δ, which means that the coherent structures do not satisfy the self-similarity. In case 3 and case 4, the particle near-wall motions are progressively enhanced and the saltation trajectories are more complex compared with those in case 2. Therefore, the disruption of near-wall vortices is more remarkable (see figure 7), which leads to a higher location than that in case 2, where the self-similar hierarchy structures are disrupted. However, the LCSs overlapped again when the reference height was equal to 0.20δ in both cases, indicating that the VLSMs/LSMs in the outer region satisfied the self-similarity, as shown in figures 12(*c*) and 12(*d*). The scaling laws in case 3 and case 4 are $\gamma_l^2 = 0.302 \ln(\lambda_x/\Delta y) - 0.755$ and $\gamma_l^2 = 0.302 \ln(\lambda_x/\Delta y) - 0.72$, respectively. The AR is approximately 12.2 in case 3 and smaller than this in case 2, suggesting that the collision bounce of the particle against the solid wall reduces the AR in the outer region. The AR of 10.8 in case 4 is smaller than that in case 3 due to the addition of
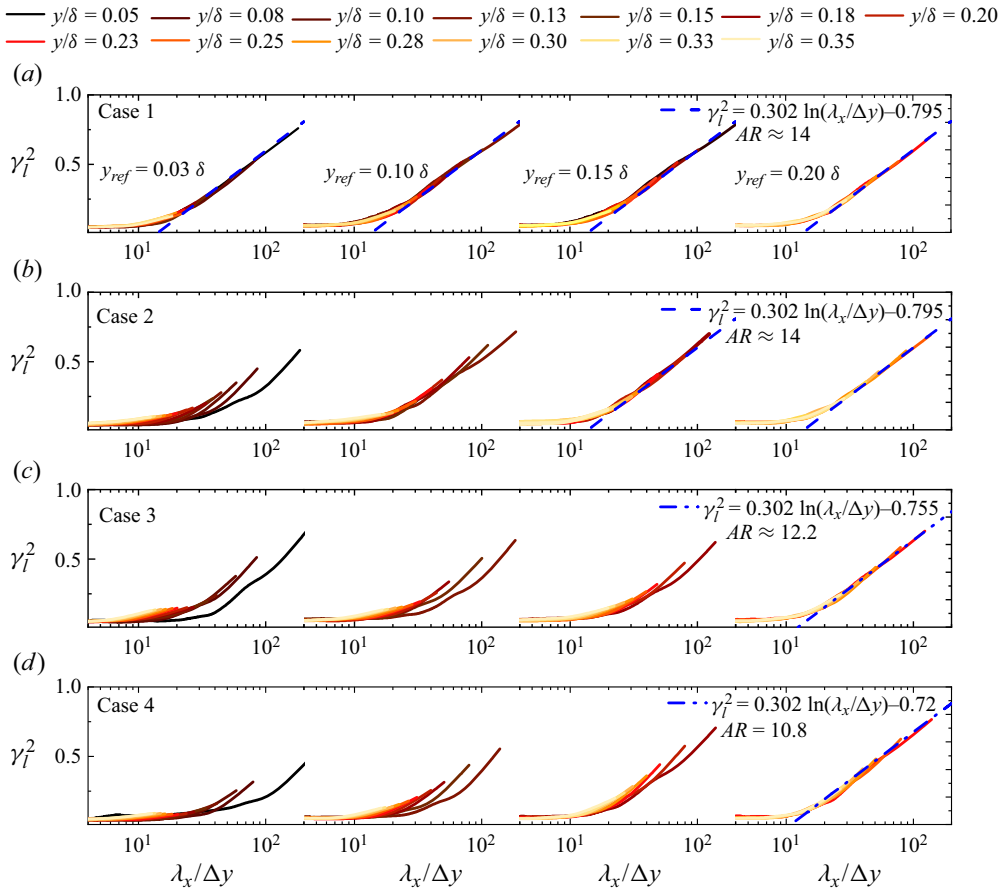
Figure 12. Variations in the turbulent LCSs at different heights for different reference heights ($y_{ref} = 0.03\delta, 0.10\delta, 0.15\delta$ and 0.20δ). The gradient colour solid lines illustrate LCSs from 0.05δ to 0.35δ. The blue dashed, dotted and dash dotted lines represent the equations: $\gamma_l^2 = 0.302\ln(\lambda_x/\Delta y) - 0.795$, $\gamma_l^2 = 0.302\ln(\lambda_x/\Delta y) - 0.755$ and $\gamma_l^2 = 0.302\ln(\lambda_x/\Delta y) - 0.72$, respectively. Cases 1–4 are displayed in (*a*–*d*), respectively.

impact splashing. Therefore, figure 12 indicates that particle collision bounce and impact splashing reduce the ARs of the streamwise/wall-normal direction.

In summary, in the near-wall region, frequent particle–wall collisions, a complex saltation trajectory and near-wall motions break down the wall-attached structures and lead to the non-coincidence of LCSs at different heights, which destroys the similarity of the coherent structure. In the outer region, the with and without particle near-wall motions do not change the similarity of coherent structures but reduce the streamwise/wall-normal AR.

When the structural morphology satisfies the similarity, the ARs of the multiscale structure are the same, which means that the coherent structure inclination angles at different scales are the same. Therefore, it is possible to verify whether the coherent structures satisfy similarity by their inclination angle at various scales for different sand-laden cases.
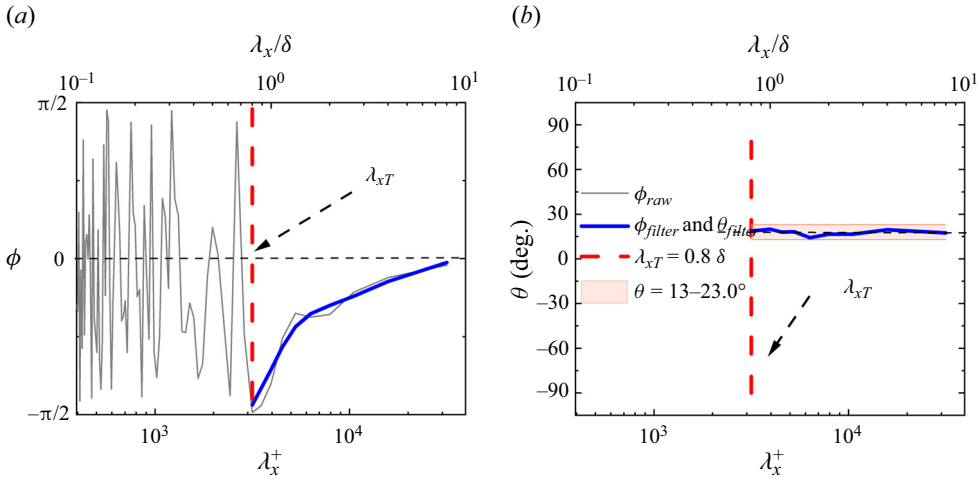
981 A26-22

Figure 13. Case 1 with $y = 0.05\delta$ for the particle-free condition: (*a*) system phase expressed as an angle and (*b*) filtered phase expressed as a physical inclination angle to 30 % BMF and then truncated by a wavelength of $\lambda_{xT} = 0.8\delta$. The red dashed line presents the truncated wavelength, the blue line represents the smoothed angle and the solid grey line shows the raw result.

The scale-dependent phase (ϕ) is represented by the real and imaginary parts of the phase to the cross-spectrum, which is given as

$$\phi = \arctan \left(\frac{\mathrm{Re} \left(\left\langle \hat{U}(y; \lambda_x) \, \hat{U}'\left(y_{ref}; \lambda_x\right) \right\rangle \right)}{\mathrm{Im} \left(\left\langle \hat{U}(y; \lambda_x) \, \hat{U}'\left(y_{ref}; \lambda_x\right) \right\rangle \right)} \right). \tag{5.4}$$

Figure 13(*a*) illustrates the phase ϕ at $y = 0.05\delta$ in the particle-free case, which can be used to extract inclination angles θ for different scales of structures on a step-by-step basis (as depicted in figure 13*b*). Combining the inclination calculation formula of $\theta = \tan^{-1}(\Delta y / \Delta x)$ and (5.4), we obtained the following equation for calculating the structure inclination:

$$\theta = 180/\pi \, \tan^{-1} \left[\frac{\Delta y}{\lambda_x} \frac{1}{(\phi/2\pi)} \right] = 180/\pi \, \tan^{-1} \left[\frac{2\pi}{\phi \, (\lambda_x/\Delta y)} \right]. \tag{5.5}$$

The phase angles acquired in this study were obtained via the approach proposed by Baars *et al.* (2016), and the corresponding results are illustrated in figure 13(*a*). The original signal was truncated and filtered with a truncated wavelength of $\lambda_{xT} = 0.8\delta$. Subsequently, the truncated signal was subjected to a smoothing process, resulting in the data represented by the blue curve in figure 13(*a*). Applying (5.5) to the blue curve data in figure 13(*a*), the structure inclination angles at different large-scale ranges are obtained (blue curve in figure 13*b*). In figure 13(*b*), the deviation of θ in case 1 is within the range of $13°$ to $23°$ (the pink area), which is agreement well with the results in particle-free flows in Chauhan *et al.* (2013) and Wu & Christensen (2010).

Figure 14(*a*) demonstrates the structural inclination angle at different scales at the same height for the four cases of the experiments. In case 1, the different scales are essentially constant at the corresponding structure inclination angle, which is essentially $15°$. This result is also consistent with the results of Baars & Marusic (2020*a*) and Li *et al.* (2022). Combined with the constant value of the streamwise/wall-normal AR obtained
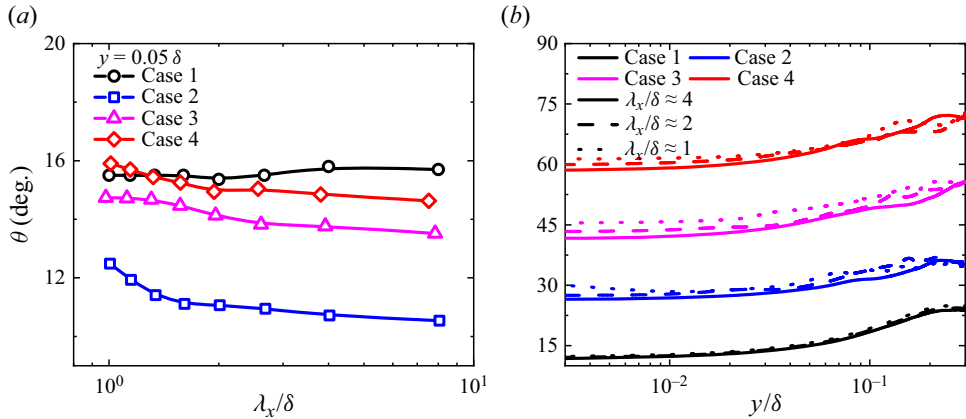
Figure 14. (*a*) Inclination at different scales for the same height ($y = 0.05\delta$) for the four cases, with black, blue, pink and red solid lines for cases 1, 2, 3 and 4, respectively. (*b*) Inclination at different scales ($\lambda_x/\delta \approx$ 4, 2, 1) for the four cases as a function of height, with each case having a $15°$ increment over the previous case. The black, blue, pink and red lines show the results for cases 1, 2, 3 and 4, respectively, while the solid, dashed and dotted lines represent the inclination of the structure for scales $\lambda_x/\delta \approx$ 4, 2 and 1, respectively.

in figure 12(*a*), the coherent structure at different scales in case 1 in the TBL satisfies self-similarity, which is consistent with the previous results (Deshpande *et al.* 2019; Baars & Marusic 2020*a*; Deshpande *et al.* 2021).

In case 2, as the blue squares in the figure 14(*a*) display, the structural inclination angles at different scales are all smaller than the case 1 results and follow a trend of log–linear decrease with scale. Near the wall, the top-released particles weaken the turbulent 'ejection and sweep' motion (Li *et al.* 2012; Liu *et al.* 2022), reducing the strength and diameter of the vortices (Lee & Lee 2019), and impacting the spacing and number of hairpin vortices in the packet (as displayed in figure 6*b*). Therefore, the self-similar structure that formed by the hairpin vortices is significantly affected, contributing to the change of inclination angle.

The pink triangles in figure 14(*a*) display the angles with different scales at the same height under case 3, and the trend of the inclination angles approximately satisfies the logarithmic increase with the scale. When comparing the results of case 2 with case 3, the inclination angle slightly increases at different scales in case 3, providing further evidence supporting that collision bounce increases the angle. The inclination angles of the large-scale structure at different scales for case 4 are displayed in the red diamonds in figure 14(*a*), where the inclination angle decreases log–linearly with scale. The inclination angles of the structures at different scales in case 4 further increased when compared with the results in case 3, indicating that impact splashing also increases the inclination angle of the coherent structures.

Figure 14(*b*) shows the inclination angle with different scales at varying heights in four cases, with each case having a $15°$ increment over the previous case. The solid, dashed and dotted lines represent the inclination angle for structures with scales $\lambda_x/\delta \approx$ 4, 2 and 1, respectively. The black curve in figure 14(*b*) illustrates the variation in the structure inclination angle concerning height in case 1, which follows a logarithmic increase scaling. The different scales of structure inclination angles predominantly coincide with each other, indicating that the large-scale structure satisfies the structure similarity (Deshpande *et al.* 2022). This result is also consistent with the field observations of Li *et al.* (2022).

981 A26-24

The blue curve in the diagram indicates that, in case 2, the variation in θ at varying scales for height follows an approximately log increase relationship. However, the variation curves in the structure inclination angle at different scales concerning height no longer overlap, suggesting the dissatisfaction of the self-similarity. The pink and red curves in figure 14(*b*) illustrate the shift in θ with height at different scales for case 3 and case 4. Similar to the results for case 1 and case 2, θ increases logarithmically with height, with smaller-scale structures corresponding to a higher inclination angle. The particle collision bounce and impact splashing significantly inhibit the bursting process (Li *et al.* 2012; Zheng *et al.* 2021; Liu *et al.* 2022), resulting in the inhibition of the generation and growth of attached coherent structures in the near-wall region, changing the θ at different scales. Accordingly, the self-similarity of the near-wall-attached coherent structure is disrupted.

6. Conclusions and discussion

This experiment focuses on the effect of the near-wall motion on the turbulent coherent structure in a two-dimensional dilute ($\Phi_v \sim 10^{-4}$) gas–solid two-phase velocity field at a moderate friction Reynolds number ($Re_\tau = 3950$). The primary objective of this study is to provide a deeper understanding of the effect of highly inertial sand particle motions on the coherent structures in two-phase flows. Simultaneous two-dimensional PIV/PTV measurements with a relatively large field of view ($8\delta \times 1.4\delta$) facilitate the simultaneous resolution of VLSMs and small-scale structures, enabling the analysis of the modulation of multiscale coherent structures by particles, collision bounce and impact splashing.

In the inner region, the top-released and bottom-released particles collided with the wall and rebounded, destroying the wall-attached vortex and disrupting the coherent structures. Therefore, the intensity of the vortex and the scale of the coherent structure are both reduced. This weakening effect is even more pronounced when the particle bottom-release case is considered in the case of impact splashing. In the outer region, the top-released particles are transported uniformly into the free stream and settled by gravity, decreasing the intensities of the 'ejection and sweep' (Liu *et al.* 2022), therefore the high- and low-velocity iso-momentum zones and the hairpin vortices are weakened, and the downward-moving particles exert a force towards the wall and reduce the inclination. However, the settling particles contribute to a stronger relationship between velocity fluctuation and an increase in the length scale of VLSMs/LSMs. The bottom-released particles enhanced the transport of energy between the inner and outer regions due to a higher proportion of ascending particles (Liu *et al.* 2022), thus, the large-scale structures and hairpin vortices are strengthened. The upward-moving particles generated by collision bounce and impact splashing represent a force away from the wall, increasing the structure's inclination and reducing its length.

Particles and particle motions affect not only the average structure but also the structure at different scales. In the near-wall region, the LCSs of different sand-laden flows do not overlap, and the inclination angles are inconsistent at different scales. In case 2, the particles collide with the wall and bounce, disrupting wall-attached structures and thus the similarity of coherent structures. In case 3, the particles are rolled up from the surface, then collide with the wall by gravity and rebound and undergo a long saltation, which disrupts the generation of the attached vortex structures (figure 6*c*), destroying the similarity of the structures. For case 4, the particle impact splashing intensifies the disruption of the vortices, disrupting the similarity of the wall-attached vortex, with different scales affected to different degrees. As a result, the streamwise/wall-normal ARs are no longer the same at different scales, and the structures do not have the same inclination. In the outer region,

the particles and particle near-wall motion do not change the similarity of the coherent structures, but the particle near-wall motion reduces the AR.

This study reveals the differences in the impacts of the particles and the particle near-wall motion on the turbulent mean structure scale, inclination and the coherent structures' self-similarity. This experiment is based on two-dimensional two-phase flow experiments; thus, only two-dimensional data are applicable. Further research is needed to determine whether the conclusions can be applied to three-dimensional flow fields. In addition, although the effects of particle–particle collision and roughness are excluded as far as possible in this study, further work is needed to refine the flow response to a set of different boundary conditions.

Supplementary movie. Supplementary movie is available at https://doi.org/10.1017/jfm.2024.65.

Author ORCIDs.

- ⓘ Yuen Feng https://orcid.org/0000-0002-1433-5050;
- ⓘ Hongyou Liu https://orcid.org/0000-0002-2444-543X;
- ⓘ Xiaojing Zheng https://orcid.org/0000-0002-6845-2949.

REFERENCES

ADRIAN, R.J., CHRISTENSEN, K.T. & LIU, Z.C. 2000 Analysis and interpretation of instantaneous turbulent velocity fields. *Exp. Fluids* **29** (3), 275–290.

BAARS, W.J., HUTCHINS, N. & MARUSIC, I. 2016 Spectral stochastic estimation of high-Reynolds-number wall-bounded turbulence for a refined inner-outer interaction model. *Phys. Rev. Fluids* **1** (5), 054406.

BAARS, W.J., HUTCHINS, N. & MARUSIC, I. 2017*a* Reynolds number trend of hierarchies and scale interactions in turbulent boundary layers. *Phil. Trans. R. Soc. Lond.* A **375** (2089), 20160077.

BAARS, W.J., HUTCHINS, N. & MARUSIC, I. 2017*b* Self-similarity of wall-attached turbulence in boundary layers. *J. Fluid Mech.* **823**, R2.

BAARS, W.J. & MARUSIC, I. 2020*a* Data-driven decomposition of the streamwise turbulence kinetic energy in boundary layers. Part 1. Energy spectra. *J. Fluid Mech.* **882**, A25.

BAARS, W.J. & MARUSIC, I. 2020*b* Data-driven decomposition of the streamwise turbulence kinetic energy in boundary layers. Part 2. Integrated energy and A_1. *J. Fluid Mech.* **882**, A26.

BAIDYA, R., PHILIP, J., HUTCHINS, N., MONTY, J.P. & MARUSIC, I. 2019 Spatial averaging effects on the streamwise and wall-normal velocity measurements in a wall-bounded turbulence using a cross-wire probe. *Meas. Sci. Technol.* **30** (8), 085303.

BAKER, L.J. & COLETTI, F. 2021 Particle–fluid–wall interaction of inertial spherical particles in a turbulent boundary layer. *J. Fluid Mech.* **908**, A39.

BERK, T. & COLETTI, F. 2020 Transport of inertial particles in high-Reynolds-number turbulent boundary layers. *J. Fluid Mech.* **903**, A18.

BHAGANAGAR, K., KIM, J. & COLEMAN, G. 2004 Effect of roughness on wall-bounded turbulence. *Flow Turbul. Combust.* **72** (2–4), 463–492.

CHAUHAN, K., HUTCHINS, N., MONTY, J. & MARUSIC, I. 2013 Structure inclination angles in the convective atmospheric surface layer. *Boundary-Layer Meteorol.* **147**, 41–50.

CHRISTENSEN, K.T. & ADRIAN, R.J. 2001 Statistical evidence of hairpin vortex packets in wall turbulence. *J. Fluid Mech.* **431**, 433–443.

CLAUSER, F.H. 1956 The turbulent boundary layer. *Adv. Appl. Mech.* **4**, 1–51.

COSTA, P., BRANDT, L. & PICANO, F. 2021 Near-wall turbulence modulation by small inertial particles. *J. Fluid Mech.* **922**, A9.

981 A26-26

Cui, G., Ruhman, I. & Jacobi, I. 2022 Spatial detection and hierarchy analysis of large-scale particle clusters in wall-bounded turbulence. *J. Fluid Mech.* **942**, A52.

Del Álamo, J.C., Jimenez, J., Zandonade, P. & Moser, R.D. 2006 Self-similar vortex clusters in the turbulent logarithmic region. *J. Fluid Mech.* **561**, 329–358.

Dennis, D.J.C. 2015 Coherent structures in wall-bounded turbulence. *An. Acad. Bras. Ciênc.* **87**, 1161–1193.

Dennis, D.J.C. & Nickels, T.B. 2011*a* Experimental measurement of large-scale three-dimensional structures in a turbulent boundary layer. Part 1. Vortex packets. *J. Fluid Mech.* **673**, 180–217.

Dennis, D.J.C. & Nickels, T.B. 2011*b* Experimental measurement of large-scale three-dimensional structures in a turbulent boundary layer. Part 2. Long structures. *J. Fluid Mech.* **673**, 218–244.

Deshpande, R., Monty, J.P. & Marusic, I. 2019 Streamwise inclination angle of large wall-attached structures in turbulent boundary layers. *J. Fluid Mech.* **877**, R4.

Deshpande, R., de Silva, C.M., Lee, M., Monty, J.P. & Marusic, I. 2021 Data-driven enhancement of coherent structure-based models for predicting instantaneous wall turbulence. *Intl J. Heat Fluid Flow* **92**, 108879.

Deshpande, R., de Silva, C.M. & Marusic, I. 2022 Evidence that turbulent superstructures are concatenations of geometrically self-similar coherent motions. arXiv:2210.06039.

Dritselis, C.D. & Vlachos, N.S. 2008 Numerical study of educed coherent structures in the near-wall region of a particle-laden channel flow. *Phys. Fluids* **20** (5), 055103.

Dritselis, C.D. & Vlachos, N.S. 2011 Numerical investigation of momentum exchange between particles and coherent structures in low *Re* turbulent channel flow. *Phys. Fluids* **23** (2), 025103.

Elghobashi, S. 1994 On predicting particle-laden turbulent flows. *Appl. Sci. Res.* **52**, 309–329.

Gao, W., Samtaney, R. & Richter, D.H. 2023 Direct numerical simulation of particle-laden flow in an open channel at $Re_\tau \approx 5186$. *J. Fluid Mech.* **957**, A3.

Hu, R., Yang, X.I.A. & Zheng, X. 2020 Wall-attached and wall-detached eddies in wall-bounded turbulent flows. *J. Fluid Mech.* **885**, A30.

Hunt, J.C.R., Wray, A.A. & Moin, P. 1988 Eddies, streams and convergence zones in turbulent flows. In *Proceedings of the Summer Program 1988, Center for Turbulence Research*, pp. 193–208. Stanford University.

Hutchins, N., Hambleton, W.T. & Marusic, I. 2005 Inclined cross-stream stereo particle image velocimetry measurements in turbulent boundary layers. *J. Fluid Mech.* **541**, 21–54.

Hutchins, N. & Marusic, I. 2007 Evidence of very long meandering features in the logarithmic region of turbulent boundary layers. *J. Fluid Mech.* **579**, 1–28.

Hwang, J. & Sung, H.J. 2018 Wall-attached structures of velocity fluctuations in a turbulent boundary layer. *J. Fluid Mech.* **856**, 958–983.

Jeong, J. & Hussain, F. 1995 On the identification of a vortex. *J. Fluid Mech.* **285**, 69–94.

Jeong, J., Hussain, F., Schoppa, W. & Kim, J. 1997 Coherent structures near the wall in a turbulent channel flow. *J. Fluid Mech.* **332**, 185–214.

Ji, C., Munjiza, A., Avital, E., Xu, D. & Williams, J. 2014 Saltation of particles in turbulent channel flow. *Phys. Rev.* E **89** (5), 052202.

Jie, Y., Cui, Z., Xu, C. & Zhao, L. 2022 On the existence and formation of multi-scale particle streaks in turbulent channel flows. *J. Fluid Mech.* **935**, A18.

Kadivar, M., Tormey, D. & McGranaghan, G. 2021 A review on turbulent flow over rough surfaces: fundamentals and theories. *Intl J. Thermofluids* **10**, 100077.

Kidanemariam, A.G., Chan-Braun, C., Doychev, T. & Uhlmann, M. 2013 Direct numerical simulation of horizontal open channel flow with finite-size, heavy particles at low solid volume fraction. *New J. Phys.* **15** (2), 025031.

Kidanemariam, A.G. & Uhlmann, M. 2017 Formation of sediment patterns in channel flow: minimal unstable systems and their temporal evolution. *J. Fluid Mech.* **818**, 716–743.

Kiger, K.T. & Pan, C. 2000 PIV technique for the simultaneous measurement of dilute two-phase flows. *Trans. ASME J. Fluids Engng* **122** (4), 811–818.

Kiger, K.T. & Pan, C 2002 Suspension and turbulence modification effects of solid particulates on a horizontal turbulent channel flow. *J. Turbul.* **3** (1), 019.

Kim, K.C. & Adrian, R.J. 1999 Very large-scale motion in the outer layer. *Phys. Fluids* **11** (2), 417–422.

Kline, S.J., Reynolds, W.C., Schraub, F.A. & Runstadler, P.W. 1967 The structure of turbulent boundary layers. *J. Fluid Mech.* **30** (4), 741–773.

Krug, D., Baars, W.J., Hutchins, N. & Marusic, I. 2019 Vertical coherence of turbulence in the atmospheric surface layer: connecting the hypotheses of townsend and davenport. *Boundary-Layer Meteorol.* **172** (2), 199–214.

LEE, J. & LEE, C. 2015 Modification of particle-laden near-wall turbulence: effect of Stokes number. *Phys. Fluids* **27** (2), 023303.

LEE, J. & LEE, C. 2019 The effect of wall-normal gravity on particle-laden near-wall turbulence. *J. Fluid Mech.* **873**, 475–507.

LEE, J.H. & SUNG, H.J. 2011 Very-large-scale motions in a turbulent boundary layer. *J. Fluid Mech.* **673**, 80–120.

LI, B. & MCKENNA NEUMAN, C. 2012 Boundary-layer turbulence characteristics during aeolian saltation. *Geophys. Res. Lett.* **39** (11), L11402.

LI, J., WANG, H., LIU, Z., CHEN, S. & ZHENG, C. 2012 An experimental study on turbulence modification in the near-wall boundary layer of a dilute gas-particle channel flow. *Exp. Fluids* **53** (5), 1385–1403.

LI, X., HUTCHINS, N., ZHENG, X., MARUSIC, I. & BAARS, W.J. 2022 Scale-dependent inclination angle of turbulent structures in stratified atmospheric surface layers. *J. Fluid Mech.* **942**, A38.

LIGRANI, P.M. & MOFFAT, R.J. 1986 Structure of transitionally rough and fully rough turbulent boundary layers. *J. Fluid Mech.* **162**, 69–98.

LIU, H., FENG, Y. & ZHENG, X. 2022 Experimental investigation of the effects of particle near-wall motions on turbulence statistics in particle-laden flows. *J. Fluid Mech.* **943**, A8.

LIU, H.Y., BO, T.L. & LIANG, Y.R. 2017 The variation of large-scale structure inclination angles in high Reynolds number atmospheric surface layers. *Phys. Fluids* **29** (3), 035104.

LIU, X., LUO, K. & FAN, J. 2016 Turbulence modulation in a particle-laden flow over a hemisphere-roughened wall. *Intl J. Multiphase Flow* **87**, 250–262.

LOZANO-DURÁN, A., INITSO. FLORES & JIMÉNEZ, J. 2012 The three-dimensional structure of momentum transfer in turbulent channels. *J. Fluid Mech.* **694**, 100–130.

LUO, K., WANG, Z., LI, D., TAN, J. & FAN, J. 2017 Fully resolved simulations of turbulence modulation by high-inertia particles in an isotropic turbulent flow. *Phys. Fluids* **29** (11), 113301.

MARCHIOLI, C. & SOLDATI, A. 2002 Mechanisms for particle transfer and segregation in a turbulent boundary layer. *J. Fluid Mech.* **468**, 283–315.

MARUSIC, I. 2001 On the role of large-scale structures in wall turbulence. *Phys. Fluids* **13** (3), 735–743.

MARUSIC, I., MCKEON, B.J., MONKEWITZ, P.A., NAGIB, H.M., SMITS, A.J. & SREENIVASAN, K.R. 2010 Wall-bounded turbulent flows at high reynolds numbers: recent advances and key issues. *Phys. Fluids* **22** (6), 065103.

MARUSIC, I. & MONTY, J.P. 2019 Attached eddy model of wall turbulence. *Annu. Rev. Fluid Mech.* **51**, 49–74.

MOIN, P. & KIM, J. 1985 The structure of the vorticity field in turbulent channel flow. Part 1. Analysis of instantaneous fields and statistical correlations. *J. Fluid Mech.* **155**, 441–464.

MOTOORI, Y. & GOTO, S. 2019 Generation mechanism of a hierarchy of vortices in a turbulent boundary layer. *J. Fluid Mech.* **865**, 1085–1109.

MOTOORI, Y. & GOTO, S. 2021 Hierarchy of coherent structures and real-space energy transfer in turbulent channel flow. *J. Fluid Mech.* **911**, A27.

PÄHTZ, T. & THOLEN, K. 2021 Aeolian sand transport: scaling of mean saltation length and height and implications for mass flux scaling. *Aeolian Res.* **52**, 100730.

PERRY, A.E. & CHONG, M.S. 1982 On the mechanism of wall turbulence. *J. Fluid Mech.* **119**, 173–217.

PICANO, F., BREUGEM, W.P. & BRANDT, L. 2015 Turbulent channel flow of dense suspensions of neutrally buoyant spheres. *J. Fluid Mech.* **764**, 463–487.

PORTELA, L.M. & OLIEMANS, R.V.A. 2003 Eulerian–lagrangian DNS/LES of particle–turbulence interactions in wall-bounded flows. *Intl J. Numer. Meth. Fluids* **43** (9), 1045–1065.

REVIL-BAUDARD, T., CHAUCHAT, J., HURTHER, D. & EIFF, O. 2016 Turbulence modifications induced by the bed mobility in intense sediment-laden flows. *J. Fluid Mech.* **808**, 469–484.

RIGHETTI, M. & ROMANO, G.P. 2004 Particle–fluid interactions in a plane near-wall turbulent flow. *J. Fluid Mech.* **505**, 93–121.

ROHILLA, N., ARYA, S. & GOSWAMI, P.S. 2023 Effect of channel dimensions and Reynolds numbers on the turbulence modulation for particle-laden turbulent channel flows. *Phys. Fluids* **35** (5), 053323.

SCHERER, M., UHLMANN, M., KIDANEMARIAM, A.G. & KRAYER, M. 2022 On the role of turbulent large-scale streaks in generating sediment ridges. *J. Fluid Mech.* **930**, A11.

SHAO, X., WU, T. & YU, Z. 2012 Fully resolved numerical simulation of particle-laden turbulent flow in a horizontal channel at a low Reynolds number. *J. Fluid Mech.* **693**, 319–344.

SHENG, J., MENG, H. & FOX, R.O. 2000 A large eddy PIV method for turbulence dissipation rate estimation. *Chem. Engng Sci.* **55** (20), 4423–4434.

DE SILVA, C.M., CHANDRAN, D., BAIDYA, R., HUTCHINS, N. & MARUSIC, I. 2020 Periodicity of large-scale coherence in turbulent boundary layers. *Intl J. Heat Fluid Flow* **83**, 108575.

SMITH, C.R. 1984 A synthesized model of the near-wall behavior in turbulent boundary layers. In *Proceedings of the 8th Symposium on Turbulence, Missouri*, vol. 299, p. 325. University Missouri-Rolla Rolla.

TAY, G.F.K., KUHN, D.C.S. & TACHIE, M.F. 2015 Effects of sedimenting particles on the turbulence structure in a horizontal channel flow. *Phys. Fluids* **27** (2), 025106.

TOMKINS, C.D. & ADRIAN, R.J. 2003 Spanwise structure and scale growth in turbulent boundary layers. *J. Fluid Mech.* **490**, 37–74.

TOWNSEND, A.A.R. 1976 *The Structure of Turbulent Shear Flow*. Cambridge University Press.

TUTKUN, M., GEORGE, W.K., DELVILLE, J., STANISLAS, M., JOHANSSON, P.B.V., FOUCAUT, J.M. & COUDERT, S. 2009 Two-point correlations in high Reynolds number flat plate turbulent boundary layers. *J. Turbul.* **10** (10), N21.

VOLINO, R.J., SCHULTZ, M.P. & FLACK, K.A. 2007 Turbulence structure in rough-and smooth-wall boundary layers. *J. Fluid Mech.* **592**, 263–293.

VOLINO, R.J., SCHULTZ, M.P. & FLACK, K.A. 2009 Turbulence structure in a boundary layer with two-dimensional roughness. *J. Fluid Mech.* **635**, 75–101.

WANG, G. & RICHTER, D.H. 2019 Two mechanisms of modulation of very-large-scale motions by inertial particles in open channel flow. *J. Fluid Mech.* **868**, 538–559.

WANG, L., PAN, C., WANG, J. & GAO, Q. 2022 Statistical signatures of component wall-attached eddies in proper orthogonal decomposition modes of a turbulent boundary layer. *J. Fluid Mech.* **944**, A26.

WU, X., BALTZER, J.R. & ADRIAN, R.J. 2012 Direct numerical simulation of a 30R long turbulent pipe flow at $R^+ = 685$: large-and very large-scale motions. *J. Fluid Mech.* **698**, 235–281.

WU, Y. & CHRISTENSEN, K.T. 2006 Population trends of spanwise vortices in wall turbulence. *J. Fluid Mech.* **568**, 55–76.

WU, Y. & CHRISTENSEN, K.T. 2010 Spatial structure of a turbulent boundary layer with irregular surface roughness. *J. Fluid Mech.* **655**, 380–418.

YANG, J.Q., CHUNG, H. & NEPF, H.M. 2016 The onset of sediment transport in vegetated channels predicted by turbulent kinetic energy. *Geophys. Res. Lett.* **43** (21), 11–261.

ZHANG, W., WANG, Y. & LEE, S.J. 2008 Simultaneous PIV and PTV measurements of wind and sand particle velocities. *Exp. Fluids* **45** (2), 241–256.

ZHAO, L.H., ANDERSSON, H.I. & GILLISSEN, J.J.J. 2010 Turbulence modulation and drag reduction by spherical particles. *Phys. Fluids* **22** (8), 081702.

ZHENG, X., WANG, G. & ZHU, W. 2021 Experimental study on the effects of particle–wall interactions on VLSM in sand-laden flows. *J. Fluid Mech.* **914**, A35.

ZHOU, J., ADRIAN, R.J., BALACHANDAR, S. & KENDALL, T.M. 1999 Mechanisms for generating coherent packets of hairpin vortices in channel flow. *J. Fluid Mech.* **387**, 353–396.

ZHU, H., PAN, C., WANG, G., LIANG, Y., JI, X. & WANG, J. 2021 Attached eddy-like particle clustering in a turbulent boundary layer under net sedimentation conditions. *J. Fluid Mech.* **920**, A53.

ZHU, H., PAN, C., WANG, J., LIANG, Y. & JI, X. 2019 Sand-turbulence interaction in a high-Reynolds-number turbulent boundary layer under net sedimentation conditions. *Intl J. Multiphase Flow* **119** (1), 56–71.